Philip L. Cole
The George Washington University
Center for Nuclear Studies
Revised April 1996
CLAS-Note 95-005

# Calibration of the TOF System by Using Relativistic Pions Arising from the Reaction $\gamma p \rightarrow p\pi^+\pi^-$

## 1  Introduction

In this **CLAS-Note** we discuss how a fast-moving pion can be used to calibrate the TOF scintillators. We have studied the reaction $\gamma p \rightarrow p\pi^+\pi^-$ in the absence of a magnetic field under varying the incident photon energy, imposing cuts on the energy balance and the velocity of the final-state particles. We find that for the nominal angular resolutions, after the track has been smeared by multiple scattering. and for the expected energy resolution of the tagged photon, the uncertainty in timing of the relativistic pion ranges from $\sim 100$ psec to $\sim 50$ psec for incident photons in the energy range of $1.00 < E_\gamma < 2.25$ GeV. Because the uncertainty in the time of flight of the final-state pions is less than the expected intrinsic timing resolution of 150 psec for the TOF counters, these pions will serve admirably to calibrate the TOF counters.

## 2  Momentum Reconstruction and Mass-ID Algorithm

In the absence of a magnetic field, the trajectories of the charged particles will be straight lines. We will therefore not be able to ascertain either the momentum of the particle or the sign of its charge by measuring the curvature of the track. For the reaction $\gamma p \rightarrow p\pi^+\pi^-$, the complete kinematics can be determined by measuring the polar and azimuthal angles of emission ($\theta$ and $\phi$) for each track and tagging the energy of the incident photon. We demand, furthermore, that there be identically three charged particles in the final state, and that each track be measured in all three

1

wire chambers. The direction of the incident photon is along the $z$ axis, and hence $\vec{p}_\gamma = E_\gamma \hat{k}$. From the conservation of momentum

$$\begin{pmatrix} p_1 \\ p_2 \\ p_3 \end{pmatrix} = \boldsymbol{A}^{-1} \begin{pmatrix} 0 \\ 0 \\ E_\gamma \end{pmatrix} \tag{1}$$

Here, $p_i$ is the total momentum of the $i$th charged particle, and the matrix $\boldsymbol{A}$ is defined as

$$\boldsymbol{A} = \begin{pmatrix} \sin\theta_1 \cos\phi_1 & \sin\theta_1 \sin\phi_1 & \cos\theta_1 \\ \sin\theta_2 \cos\phi_2 & \sin\theta_2 \sin\phi_2 & \cos\theta_2 \\ \sin\theta_3 \cos\phi_3 & \sin\theta_3 \sin\phi_3 & \cos\theta_3 \end{pmatrix} \tag{2}$$

We now calculate the energy of each particle, which is given by

$$E_i = \sqrt{p_i^2 + m_i^2}. \tag{3}$$

We ascribe the mass of the proton or pion to $m_i$, and iterate until we find the minimum of the energy balance

$$|\Delta E| = |E_{\text{initial}} - E_{\text{final}}|, \tag{4}$$

where

$$E_{\text{initial}} = E_\gamma + m_{\text{prot}}, \tag{5}$$

and

$$E_{\text{final}} = \sum_{i=1}^{3} (\sqrt{p_i^2 + m_i^2}). \tag{6}$$

After we have determined the minimum of $|\Delta E|$, the tracks are mass identified. That is to say, we now can identify whether a track belongs to a proton or a pion. We cannot, however, distinguish between a $\pi^+$ or a $\pi^-$ track.

# 3   Acceptances

In this section we discuss the acceptances of both signal events ($\gamma p \to p\pi^+\pi^-$) and the expected background events ($\gamma p \to p\pi^+\pi^-\pi^0$ and $\gamma p \to n\pi^+\pi^+\pi^-$). We define the acceptance in the usual way

$$\varepsilon = \frac{N_{\text{acc}}}{N_{\text{gen}}}, \tag{7}$$

where $N_{acc}$ is the number of events satisfying both the software selection criteria and the geometrical acceptances, and $N_{gen}$ is the number of generated events. In our studies we found that

$$\varepsilon = \varepsilon(E_\gamma, |\Delta E|, \beta). \tag{8}$$

Here,

$E_\gamma$:     energy of the incident photon.

$|\Delta E|$:     energy balance resolution.

$\beta$:     velocity of the particle.

The events for the signal and background processes were distributed uniformly in phase space in the cms frame by using the event generator routine GENBOD from the CERNLIB software package. These generated events, in turn, were boosted to the lab frame and then processed through the CLAS simulation package FASTMC_GEN [1], which is based upon FASTMC [2].

## 3.1 Multiple Scattering and Reconstruction Mismeasurement

We must take the energy loss and the multiple scattering of the final-state protons and pions both in the LH2 target (including the walls of the containment vessel) and the detector elements properly into account. Furthermore, the nominal angular resolution of the wire chambers is 1 mrad. This means we can resolve the particle's trajectory to no better that 1 mrad. FASTMC requires that the magnetic field be nonzero in order to retrieve the smeared angle information. Before we could start our $B = 0$ studies, we first needed to determine the rms angular uncertainty, i.e., $\sigma_{\Delta\theta}$ and $\sigma_{\Delta\phi}$, as a function of particle type and 3-momentum. For both our proton and pion studies, we generated 50 000 events for each 3-momentum bin. We employed a rather involved algorithm for extracting the angular uncertainty of the proton or pion track binned in terms of 3-momentum. We first sampled the $1/E_\gamma$ spectrum using a Monte-Carlo rejection algorithm to extract the probability distribution for the bremsstrahlung photons. This sampled photon was then used to calculate the center-of-mass energy available (i.e., $\sqrt{s} = [m_p^2 + 2m_p E_\gamma]^{\frac{1}{2}}$) for producing the two-pion and proton final state. These final-state particles, in turn, were uniformly distributed in phase space in the cms frame, and then boosted to the lab frame. If the 3-momentum in the lab frame of a given pion, say, fell within the $j$th 3-momentum bin, the entire event would be written to the $j$th output event data file. Next, these properly binned events were processed through the CLAS detector simulation package, FASTMC_GEN. We set the magnetic field to positive polarity and

full strength ($B = +1B_\circ$) to maximize acceptance of positive particles and minimize the $\delta p$ error in momentum reconstruction, where

$$\delta p = [(\delta p_{\text{ms}})^2 + (\delta p_{\text{trk}})^2)]^{\frac{1}{2}}.$$

The first term arises from multiple scattering and the second term results from the intrinsic resolution of the track. We mention, parenthentically, that our results compare favorably with a GEANT study of multiple scattering in the Saclay LH2 target, including the walls [3].

Our results for the rms uncertainty in the polar and azimuthal angles for the pion (proton) are shown in Figs. 1a–b (Figs. 2a–b). The fitted curve that passes through the Monte-Carlo data points is a polynomial of the form

$$\sigma_{\text{angle}}(|\vec{p}|) = P_1 + P_2 \times |\vec{p}| + \exp(P_3 + P_4 \times |\vec{p}|). \tag{9}$$

The parameters, $P_i$, are determined from the optimization software package, MINUIT, so that the $\chi^2$ merit function is minimized. The error on the MC data points is purely statistical. We see in Figs. 1 and 2 that the momentum error is dominated by multiple scattering. For the pions (protons), we generated the events in the momentum range of $0.0 < |\vec{p}| \leq 1.7$ GeV/c ($0.2 < |\vec{p}| \leq 2.0$ GeV/c) having a bin width fixed at 0.1 GeV/c. We require that the particle travel through all three sets of wire chambers and deposit energy in the TOF counter. Low momentum protons will range out, explaining the lower bound of 200 MeV/c for the proton momentum. We expect pions decaying into muons to be a second order effect at these energies, and therefore we need not take $\pi$–$\mu$ misidentification into consideration. Now that we have a quantitative description of the smearing due to multiple scattering and track reconstruction mismeasurement, we are in the position to continue our TOF calibration studies at $B = 0$.

## 3.2 Smearing of the Track's Momentum

In the absence of a magnetic field, the radius of curvature of the final-state particles will necessarily be infinite. Hence, FastMC will not be able to ascertain the momentum of the particle by measuring the particle's curvature. However, FastMC will still provide the overall geometrical acceptance, detector response, and will indicate whether the particle has ranged out or decayed. After processing the event through FastMC, we endow the correct polar and azimuthal angular
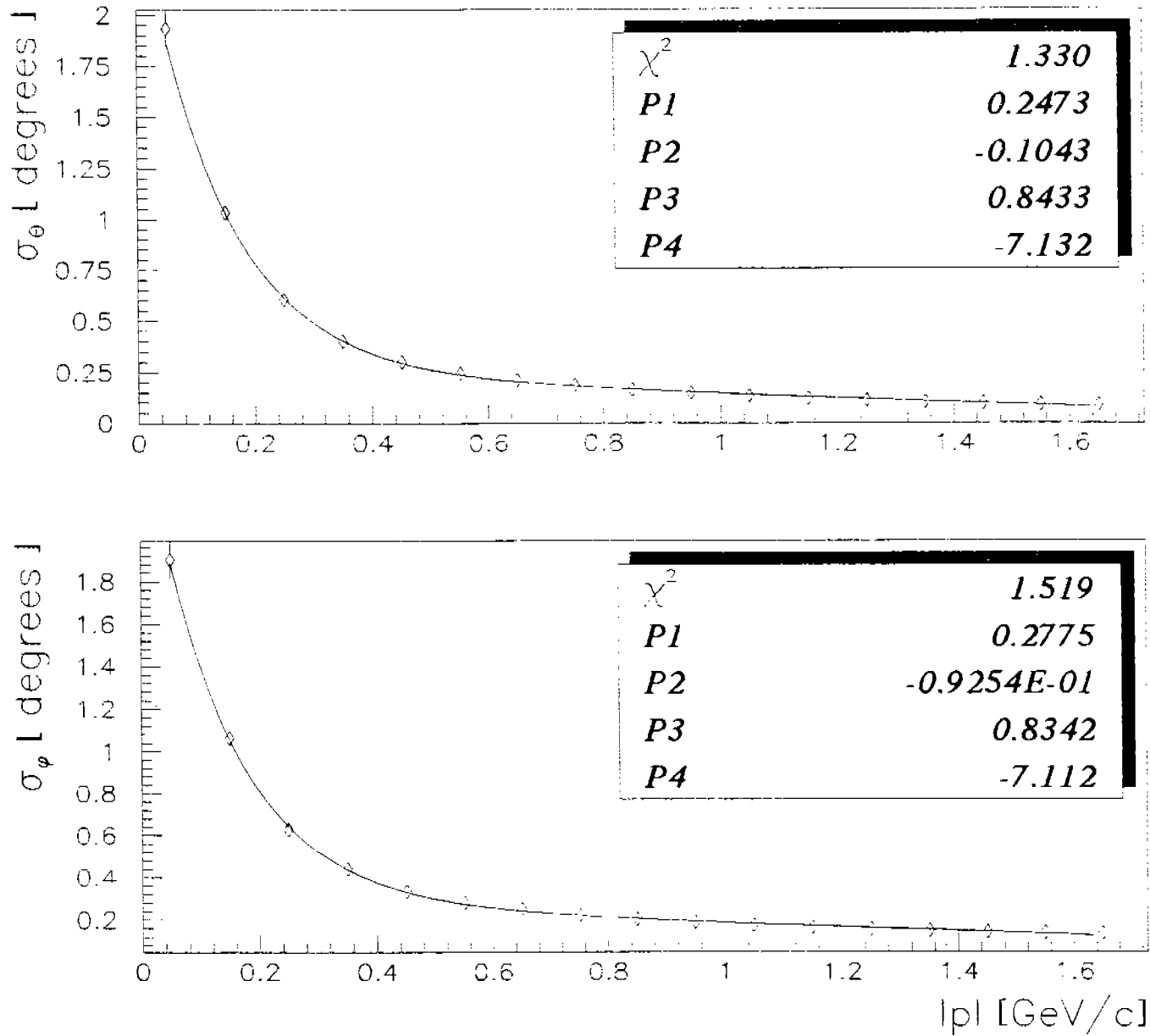
4

## Angular Resolution for pions



| $\chi^2$ | 1.330 |
|----|----|
| P1 | 0.2473 |
| P2 | -0.1043 |
| P3 | 0.8433 |
| P4 | -7.132 |

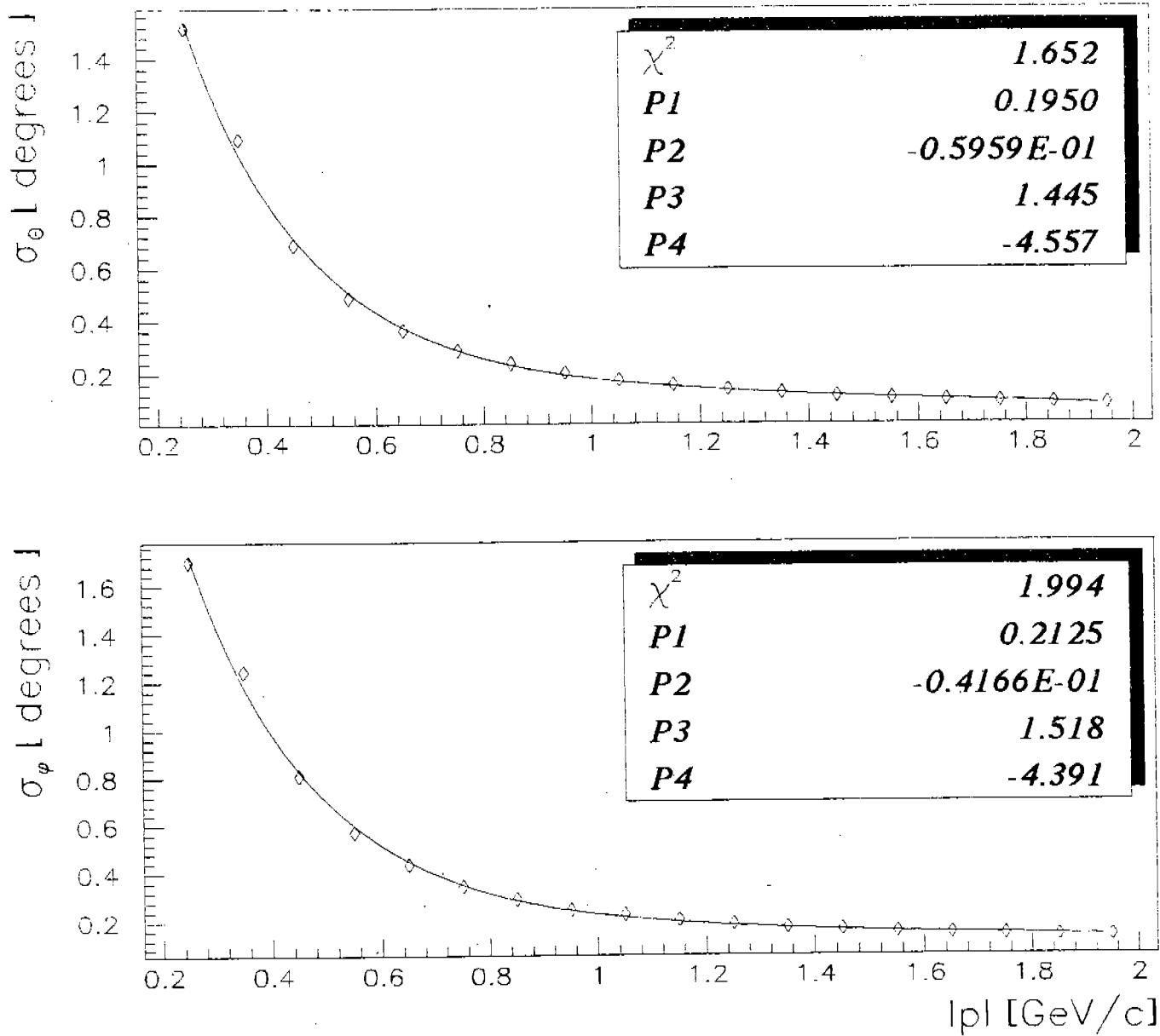| $\chi^2$ | 1.519 |
|----|----|
| P1 | 0.2775 |
| P2 | -0.9254E-01 |
| P3 | 0.8342 |
| P4 | -7.112 |

|p| [GeV/c]

Figure 1: Angular resolution of the $\pi$ track as a function of momentum. The fitted curve: $\sigma_{\mathbf{angle}}(|\vec{p}| = P_1 + P_2 \times |\vec{p}| + \exp(P_3 + |\vec{p}| \times P_4)$. (top) $\sigma_\theta^\pi = \sigma_\theta^\pi(|\vec{p}|)$, and (bottom) $\sigma_\phi^\pi = \sigma_\phi^\pi(|\vec{p}|)$.

## Angular Resolution for protons



Figure 2: Angular resolution of the proton track as a function of momentum. The fitted curve: $\sigma_{\mathbf{angle}}(|\vec{p}| = P_1 + P_2 \times |\vec{p}| + \exp(P_3 + |\vec{p}| \times P_4)$. **(top)** $\sigma_\theta^{\mathrm{prot}} = \sigma_\theta^{\mathrm{prot}}(|\vec{p}|)$, and **(bottom)** $\sigma_\phi^{\mathrm{prot}} = \sigma_\phi^{\mathrm{prot}}(|\vec{p}|)$.

smearing (see eqn. 9) to the pion and proton to obtain the rms uncertainty of the track's angle ($\sigma_\theta$ and $\sigma_\phi$) as a function of its 3-momentum, $|\vec{p}|$. We then extract the smeared angular values ($\Delta\theta$ and $\Delta\phi$) from randomly sampling a gaussian probability distribution, which is characterized by the standard deviation, $\sigma_{\text{angle}}$. We then add this smeared value to the true value of the angle, and obtain the *measured* value,

$$\theta_{\text{meas}} = \theta_{\text{true}} + \Delta\theta$$
$$\phi_{\text{meas}} = \phi_{\text{true}} + \Delta\phi. \tag{10}$$

These *measured* $\theta$s and $\phi$s for the pion and proton tracks are then used to calculate the matrix elements of $\boldsymbol{A}$ in eqn. 2. Subsequently, we can calculate the simulated experimental smearing of the components of the track's momentum from eqn. 1.

## 3.3 Signal

Our acceptance studies for the signal process were binned in terms of the incident photon energy, energy balance resolution, and the velocity cut of the measured track in the drift chambers.

$E_\gamma$:    0.5, 0.6, 0.7, 0.8, 0.9, 1.0, 1.1, 1.2, 1.5, 1.8, 2.1, and 2.4 GeV

$|\Delta E|$:    5.0, 10.0, and 20.0 MeV

$\beta_{\text{cut}}$:    0.0 and 0.75

We have, then, $12 \times 3 \times 2 = 72$ bins in all. For each bin, we generated a total of 50 000 events. For an accepted event we require that

1. three and only three charged particles be measured in the final state.

2. each track be measured in all three wire chambers.

3. at least one track associated with the pion deposit energy in a TOF counter.

4. the energy balance be within a certain value, i.e., $|\Delta E| < E_{\text{min}}$.

In Fig. 3, we show a typical track in the CLAS detector. From this figure, one can see the geometry, positioning of the various detector elements, and the scale of the CLAS. In Fig. 4, we show the energy balance distributions, $|\Delta E|$, for several slices in $E_\gamma$. In Table 1 we tabulate the acceptances
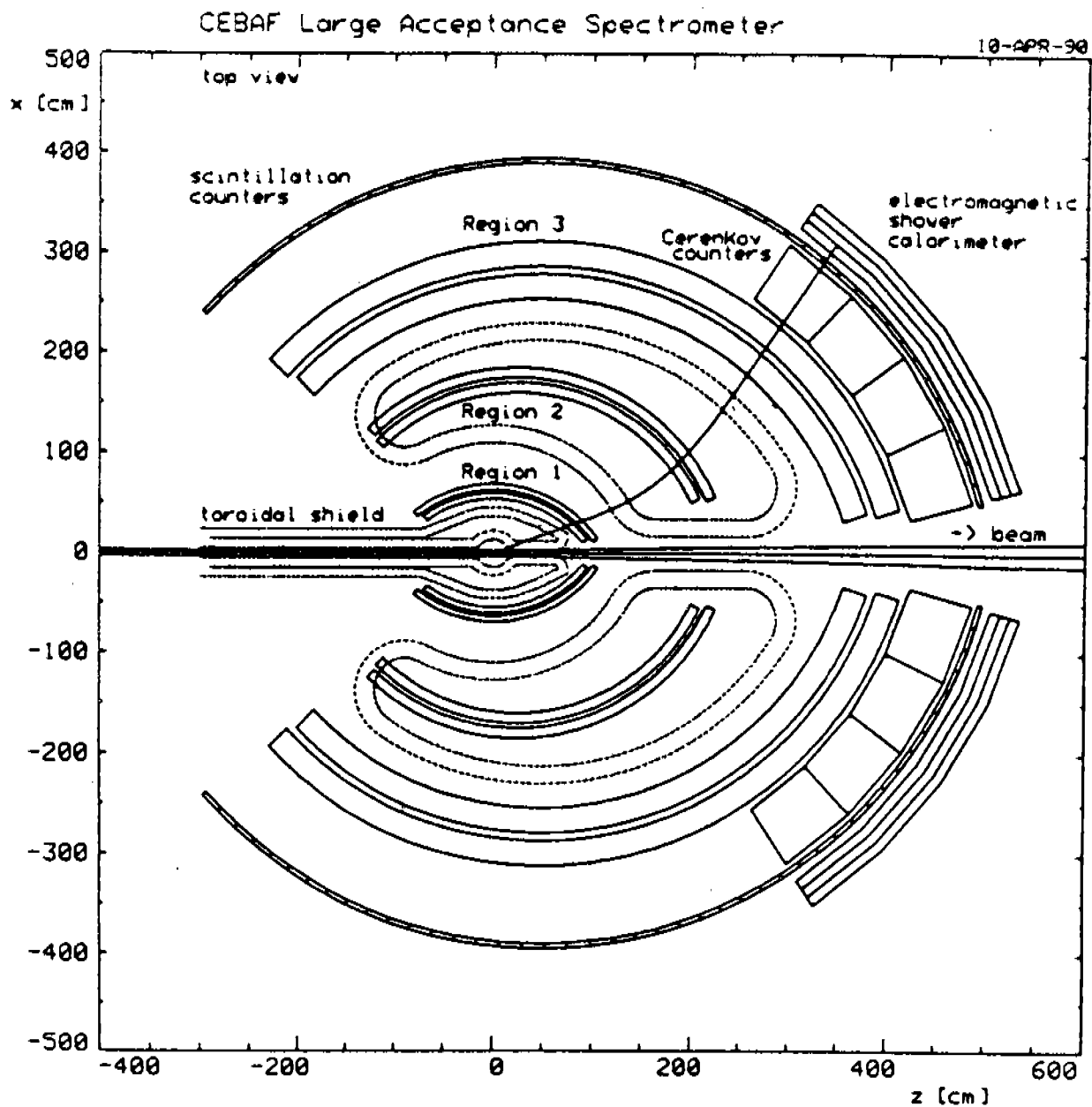
Figure 3: Midplane slice of the CLAS detector as viewed from the top. The dotted lines show the projection of the coil contours on the midplane. The trajectory of a 1 GeV/c particle is shown in a nonzero magnetic field. [This figure is from Fig. E2 of the Hall B Conceptual Design Report, April 1990].

Table 1: Acceptance of the reaction $\gamma p \to p\pi^+\pi^-$) as a function of incident photon energy, and cuts on the energy balance and velocity of the final-state particle.

| $E_\gamma$ [GeV] | $|\Delta E| \leq 5$ MeV | | | $|\Delta E| \leq 10$ MeV | | | $|\Delta E| \leq 20$ MeV | | |
|---|---|---|---|---|---|---|---|---|---|
| | No $\beta$ cut | $\beta_\pi \geq 0.75$ | $\beta_p \geq 0.75$ | No $\beta$ cut | $\beta_\pi \geq 0.75$ | $\beta_p \geq 0.75$ | No $\beta$ cut | $\beta_\pi \geq 0.75$ | $\beta_p \geq 0.75$ |
| 0.5 | 7.8% | 3.7% | – – | 10.7% | 5.0% | – – | 11.9% | 5.6% | – – |
| 0.6 | 10.7% | 7.8% | – – | 14.5% | 10.4% | – – | 15.9% | 11.4% | – – |
| 0.7 | 13.1% | 10.9% | – – | 17.3% | 14.3% | – – | 18.8% | 15.5% | – – |
| 0.8 | 15.2% | 13.4% | – – | 19.8% | 17.0% | – – | 20.9% | 18.2% | – – |
| 0.9 | 16.9% | 15.5% | – – | 20.8% | 19.0% | – – | 22.1% | 20.1% | – – |
| 1.0 | 18.2% | 16.9% | 0.1% | 21.9% | 20.4% | 0.2% | 23.1% | 21.4% | 0.2% |
| 1.1 | 19.5% | 18.4% | 0.3% | 22.9% | 21.6% | 0.4% | 24.0% | 22.6% | 0.4% |
| 1.2 | 20.0% | 19.2% | 0.6% | 23.1% | 22.1% | 0.7% | 24.0% | 23.0% | 0.7% |
| 1.5 | 21.2% | 20.7% | 1.3% | 23.5% | 22.9% | 1.5% | 24.2% | 23.5% | 1.5% |
| 1.8 | 21.1% | 20.7% | 1.9% | 22.8% | 22.4% | 2.0% | 23.4% | 23.0% | 2.1% |
| 2.1 | 20.2% | 20.0% | 2.3% | 21.5% | 21.3% | 2.4% | 22.1% | 21.8% | 2.5% |
| 2.4 | 18.9% | 18.6% | 2.5% | 19.9% | 19.7% | 2.6% | 20.4% | 20.1% | 2.7% |

as a function of incident photon energy and $|\Delta E|$ for various velocity cuts on the proton and pion. For the initial setup of the tagger, the photon is expected to be resolved to within a 0.1% uncertainty. This means that at $E_\gamma = 2.0$ GeV, the tagging resolution is expected to be 2 MeV.

The results of the acceptance studies are plotted in Figs. 5a–c, where these three plots reflect differing conditions on the energy balance resolution and velocity cuts on the final-state pions. We take Fig. 5a ($|\Delta E| = 5$ MeV) to be representative of our energy balance resolution. Fig. 6 is a magnification of Fig. 5a. In Figs. 7a–c we plot the proton acceptance for the reaction $p(\gamma,p\pi^+\pi^-)$ under various cuts. Our cuts determine the shape of the acceptance curve. For lower energies, the likelihood of all three final-state charged particles traversing all three wire chambers diminishes and hence will not pass cut 2 above, and at higher energies, the proton is boosted more forwardly in polar angle into the region where the acceptance of CLAS decreases, thereby not satisfying cut 1.

We now focus on the expected timing resolution. We first note that

$$\beta = \frac{\ell}{ct},$$

(11)

where $\ell$ is the path length. Differentiating $t$ with respect to $\beta$ yields

$$\Delta t = \frac{\ell}{c}\frac{\Delta\beta}{\beta^2}.$$

(12)

Here,

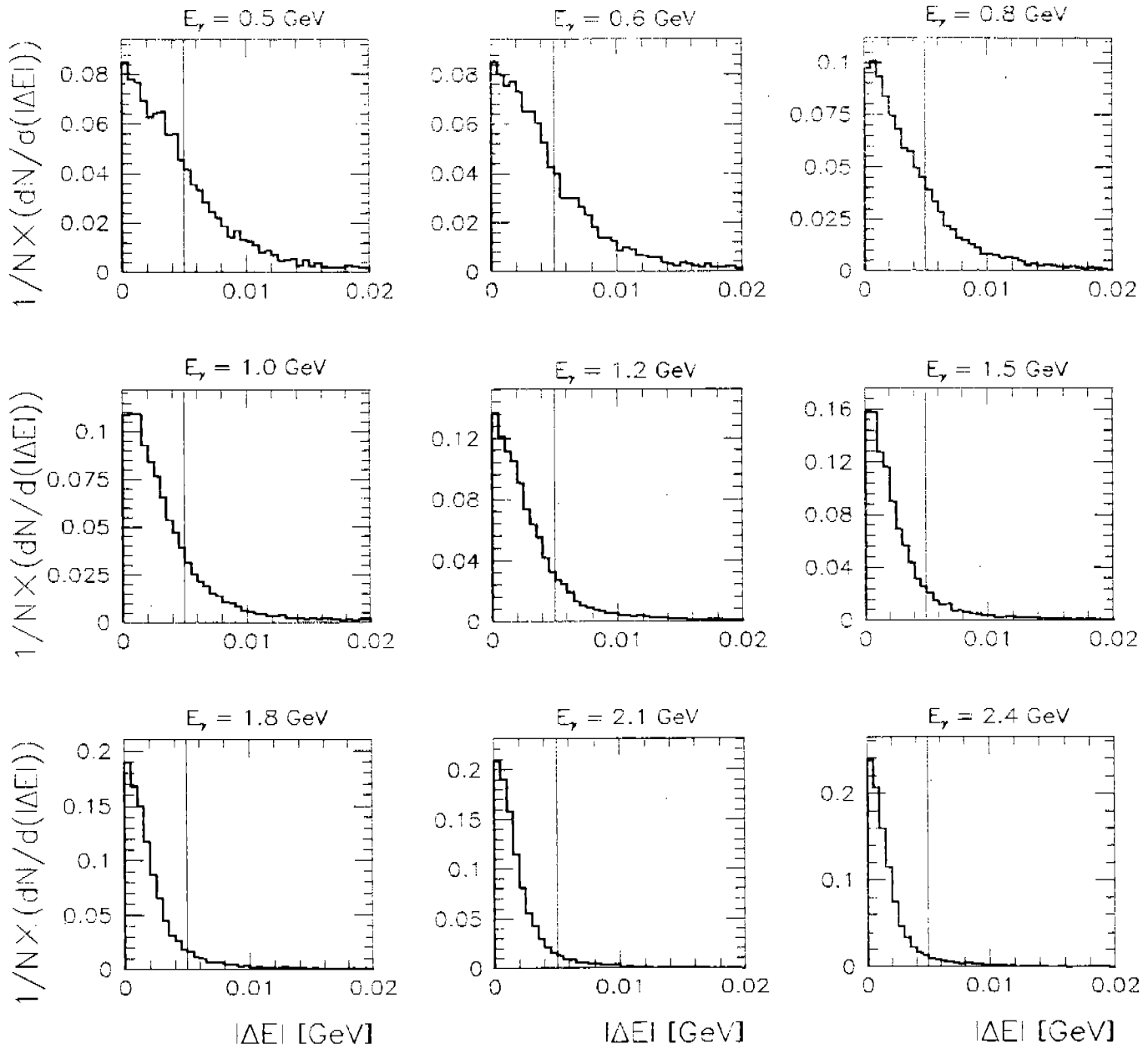$$\Delta\beta = \beta_{\text{true}} - \beta_{\text{meas}}.$$

(13)

9

Figure 4: Energy balance ($|\Delta E|$) distributions for several slices in $E_\gamma$. The distributions are normalized by area, and the vertical line is the $|\Delta E| \leq 5$ MeV cutoff.
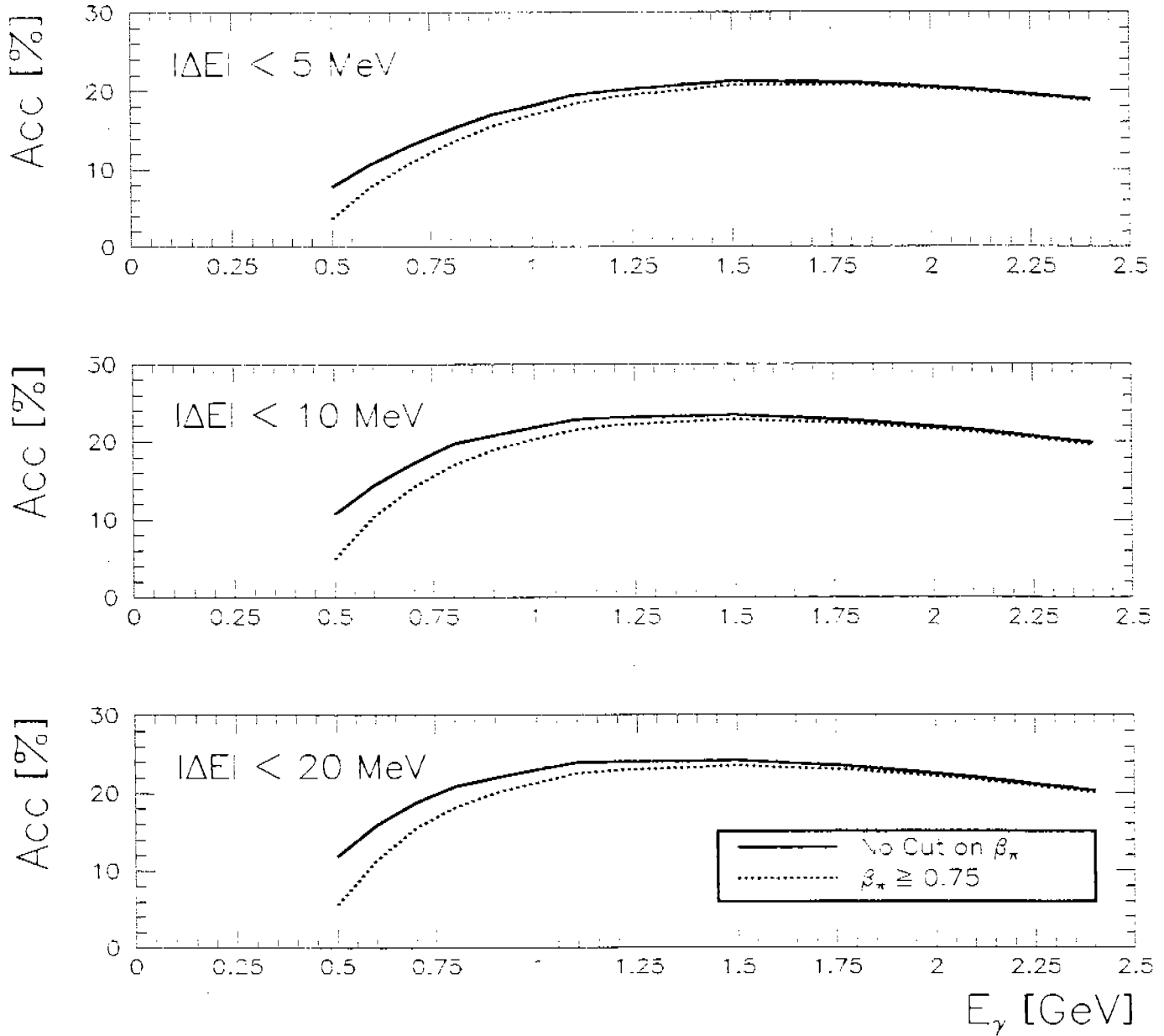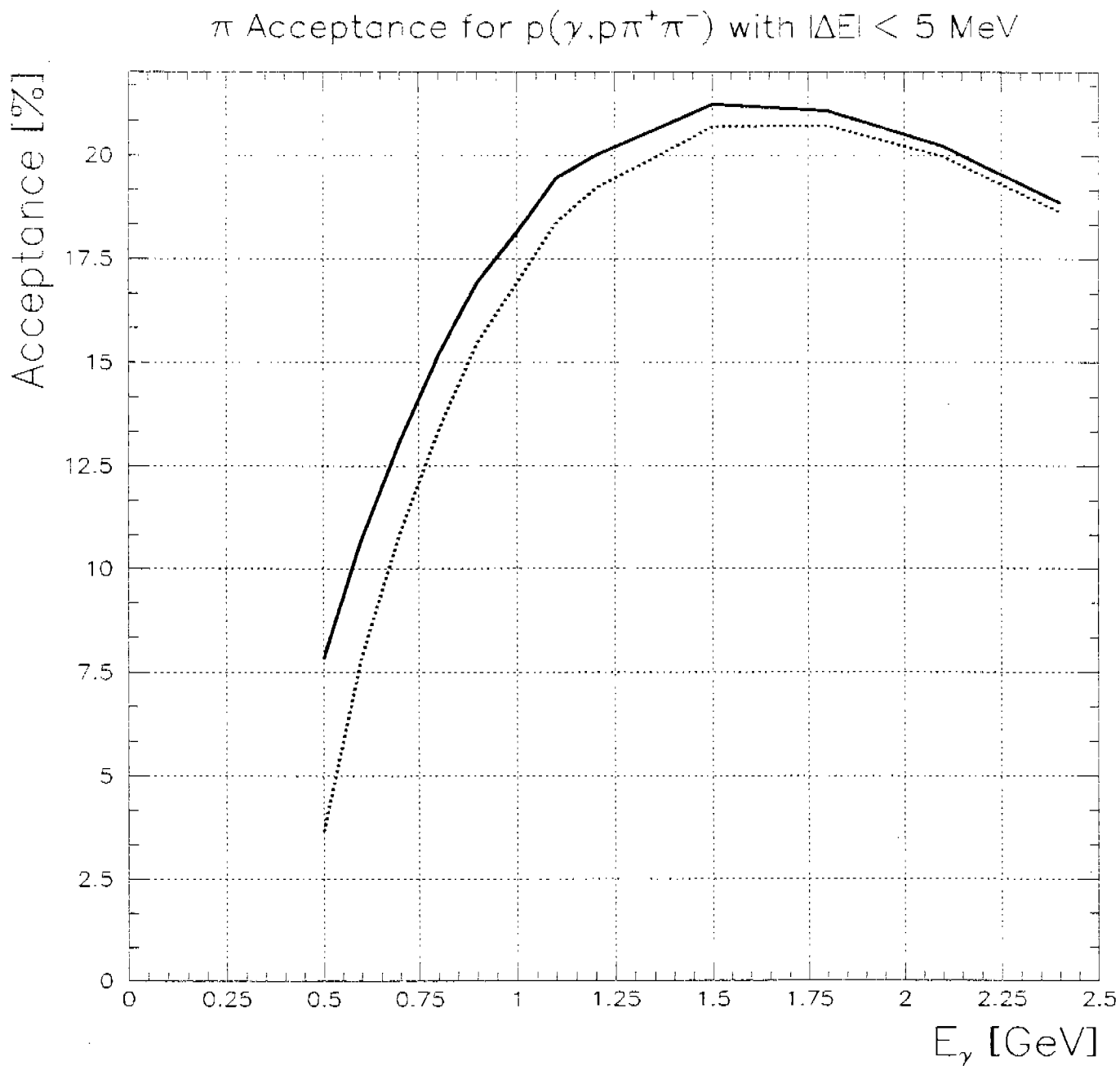
Figure 5: Acceptance of the signal $(\gamma p \rightarrow p\pi^+\pi^-$ as a function of incident photon energy and tracking angular resolution for **(a)** $|\Delta E| < 5$ MeV, **(b)** $|\Delta E| < 10$ MeV, and **(c)** $|\Delta E| < 20$ MeV, where (solid lines) no cuts on $\beta_\pi$, and (dotted lines) $\beta_\pi \geq 0.75$.

Figure 6: Acceptance of the signal $(\gamma p \rightarrow p\pi^+\pi^-)$ as a function of incident photon energy. The energy balance, $|\Delta E| < 5$ MeV. (solid line) no cuts on $\beta_\pi$, and (dotted line) $\beta_\pi \geq 0.75$. This figure is an expansion of Fig. 5a.

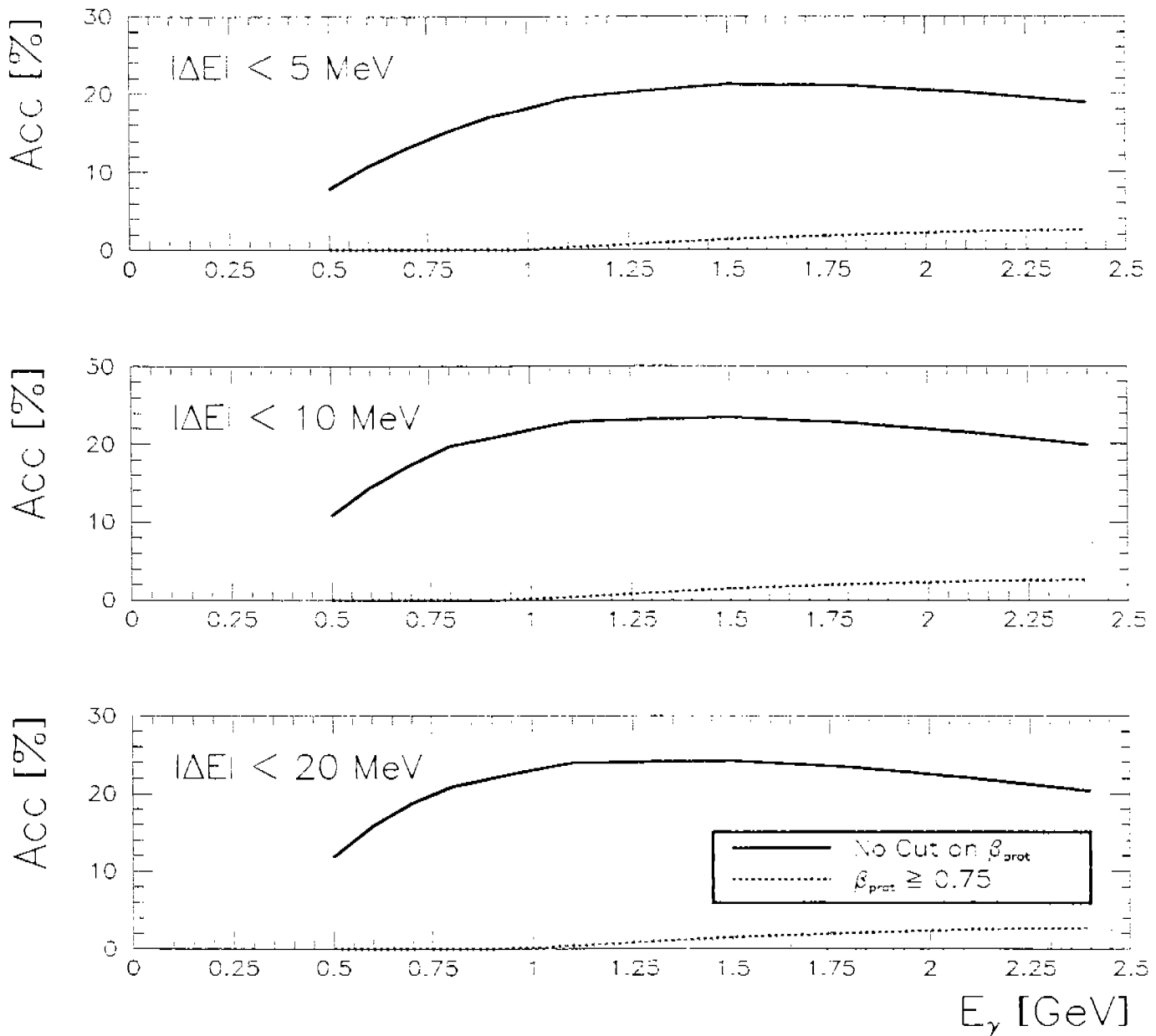## proton track acceptance from $p(\gamma, p\pi^+\pi^-)$

$|\Delta E| < 5$ MeV

$|\Delta E| < 10$ MeV

$|\Delta E| < 20$ MeV

No Cut on $\beta_{prot}$

$\beta_{prot} \geq 0.75$

$E_\gamma$ [GeV]

Figure 7: Acceptance of the signal $(\gamma p \rightarrow p\pi^+\pi^-)$ as a function of incident photon energy and tracking angular resolution for **(a)** $|\Delta E| < 5$ MeV, **(b)** $|\Delta E| < 10$ MeV, and **(c)** $|\Delta E| < 20$ MeV. where (solid lines) no cuts on $\beta_{prot}$ and (dotted lines) $\beta_{prot} \geq 0.75$. We see that there are very few fast protons.

13

The $\Delta\beta$ distributions for pions and protons for different slices in photon energy, $E_\gamma$, are shown in Fig. 8. No cuts on momentum or minimum velocity were imposed on these distributions. Since the degree of multiple scattering for a particle traversing a medium goes as the reciprocal of the product of the momentum and the velocity, slow-moving light particles will be tend to be deflected more than faster and heavier particles traversing the same medium. This effect explains the broad width of the $\Delta\beta$ distribution for $E_\gamma = 0.5$ GeV (upper left plot in Fig. 8). At lower center-of-mass energies, the acceptance criteria of requiring three charged particles in the final state, where each track traverses all three wire chambers, effectively eliminates protons having momenta less than 200 MeV/c, since these low-momentum protons will tend to range out. However, very low momentum pions will still have a high probability of making it to a TOF counter. As the center-of-mass energy increases, the partitioned energy of each of the final-state particle increases, and the pions become minimum ionizing. At higher incident photon energies the pions are deflected less, and hence, the pion $\Delta\beta$ distributions become much sharper.

The width of the $\Delta\beta$ distribution is characterized by the standard deviation

$$\sigma_{\Delta\beta} = \sqrt{\sum_{i=1}^{n} \frac{(\langle\beta\rangle - \beta_i)^2}{n-1}} \ . \tag{14}$$

We therefore define the uncertainty in the timing of the particle as

$$\sigma_{\Delta t} = \frac{\ell}{c} \cdot \frac{\sigma_{\Delta\beta}}{\langle\beta\rangle^2} \ . \tag{15}$$

From this formula, we see that to optimize the timing resolution we need to minimize the uncertainty in measuring the particle's velocity, $\sigma_{\Delta\beta}$, and preferentially select highly relativistic particles with $\beta \to 1$. In Figs. 9a–c we plot the uncertainty of the pion's velocity, $\sigma_{\Delta\beta}^\pi$, as functions of $E_\gamma$ and $|\Delta E|$. We see $\sigma_{\Delta\beta}^\pi$ improves as $E_\gamma$ increases.

In Fig. 10 we overlay the $\beta$ distributions of the pions and the protons for four different slices of $E_\gamma$, where we have invoked only the cut $|\Delta E_\gamma| < 5$ MeV, i.e., there are no conditions on the particle's velocity. We next plot the average $\beta$, $\langle\beta\rangle$, (Fig. 11a) and the rms spread, $\sigma_\beta$, (Fig. 11b) for both the measured pions and protons as a function of $E_\gamma$. We observe that $\langle\beta\rangle_\pi \sim 2\langle\beta\rangle_{prot}$ for $E_\gamma < 1.5$ GeV, and that the rms spread of the $\sigma_\beta^\pi$ is considerably narrower than for $\sigma_\beta^{prot}$ at photon energies exceeding 1.0 GeV. Because the uncertainty in the timing goes as the reciprocal of $\langle\beta\rangle^2$, the timing resolution afforded by the pion before cuts on the velocity is, on the average, approximately four times better than for the proton. Unlike the case for the protons, most of the pions survive the velocity cut of $\beta \geq 0.75$ (cf. Table 1). It is clear, then, that protons will not
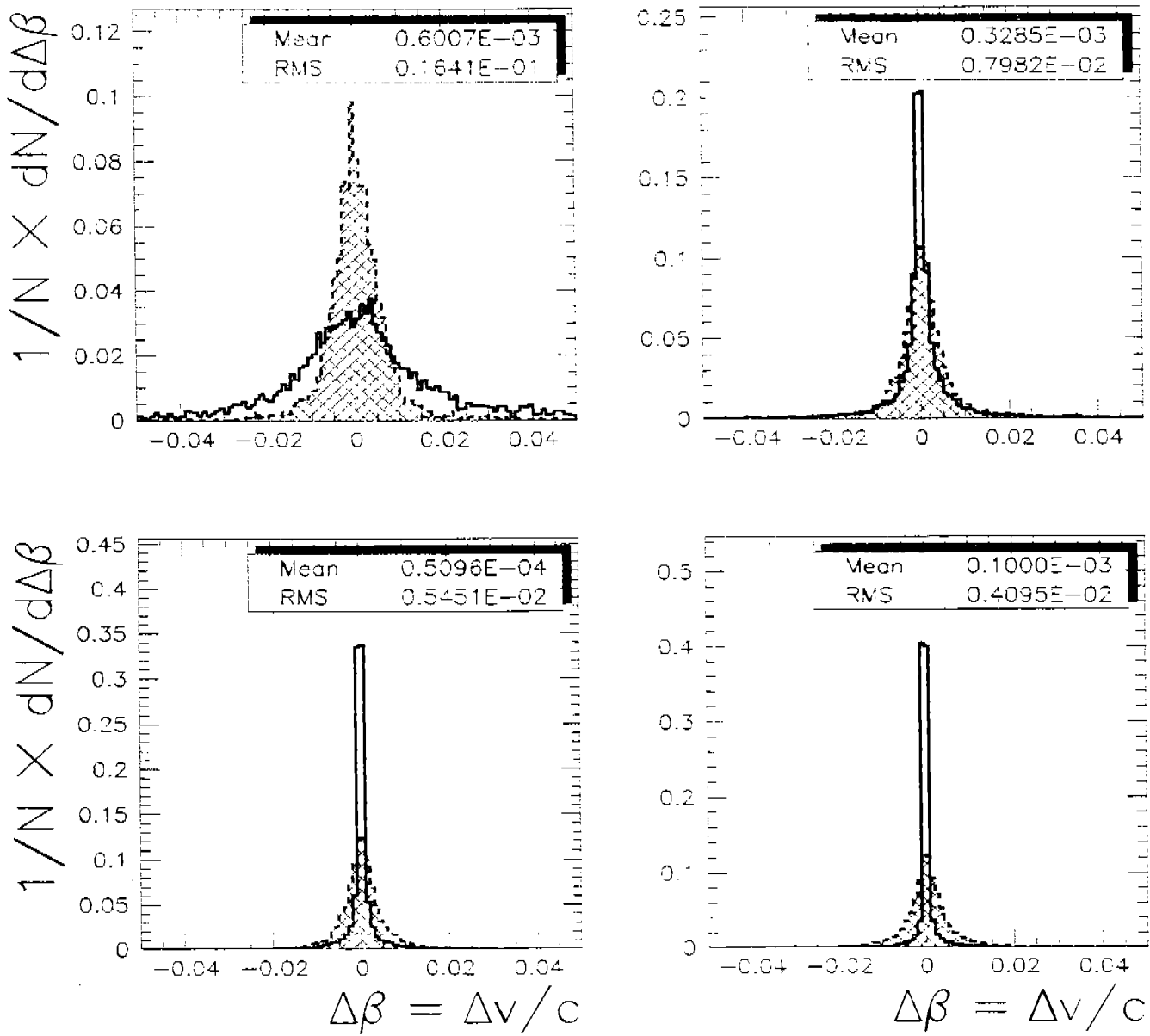
14

Figure 8: Normalized $\Delta\beta$ ($\beta_{\text{true}} - \beta_{\text{meas}}$) distributions for protons (filled-in histograms) and pions for four slices in $E_\gamma$. (upper left) $E_\gamma = 0.5$ GeV, (upper right) $E_\gamma = 1.0$ GeV, (lower left) $E_\gamma = 1.5$ GeV, and (lower right) $E_\gamma = 2.1$ GeV. The parameters in the inset boxes refer to the pion $\Delta\beta$ distributions. No cuts on the minimum velocity of the particle have been imposed.
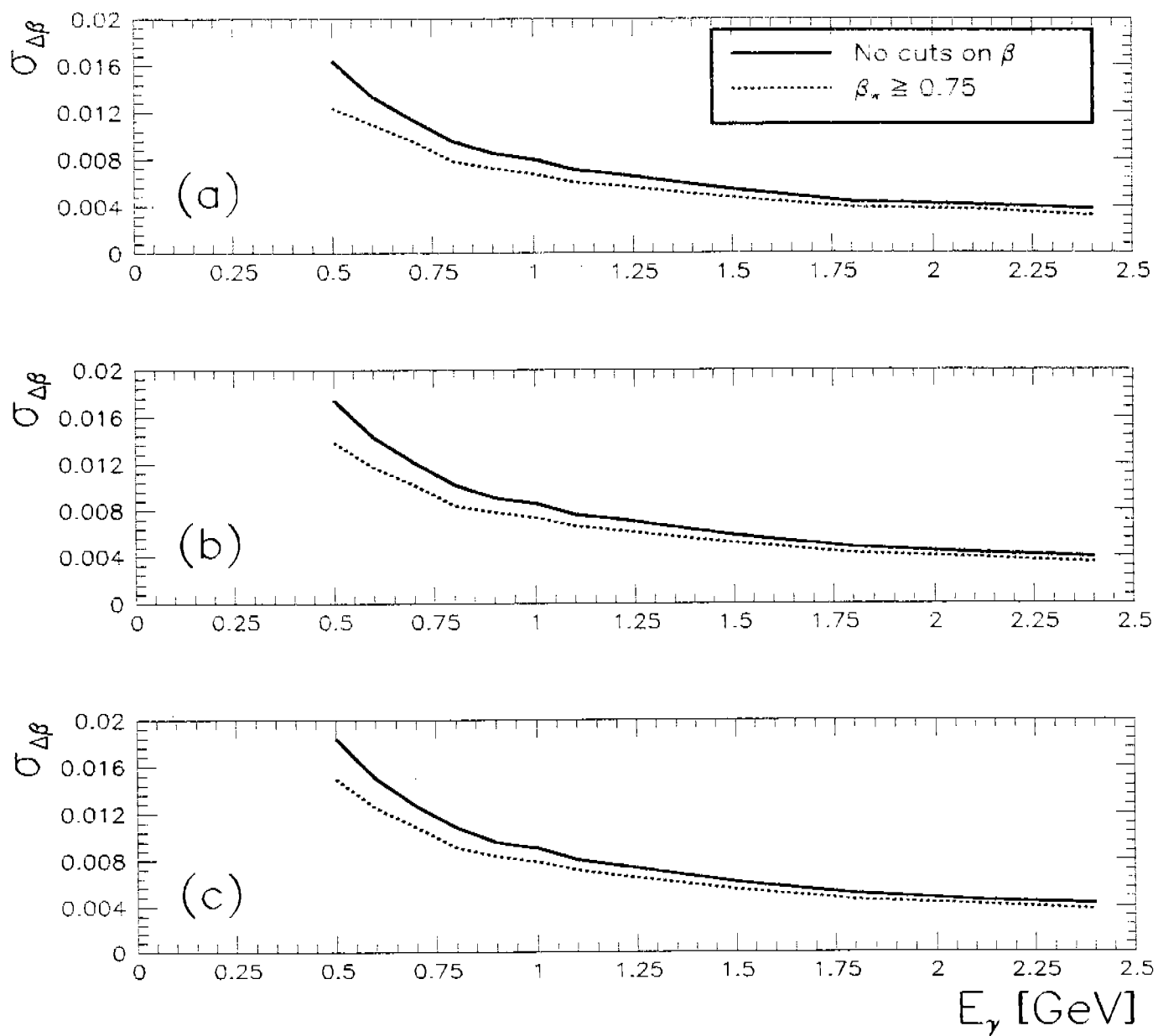
Figure 9: Resolution of the $\pi$ track's velocity, $\sigma_{\Delta\beta}$, for pions arising from $\gamma p \rightarrow p\pi^+\pi^-$ as a function of incident photon energy and tracking angular resolution for (a) $|\Delta E| < 5$ MeV, (b) $|\Delta E| < 10$ MeV, and (c) $|\Delta E| < 20$ MeV.

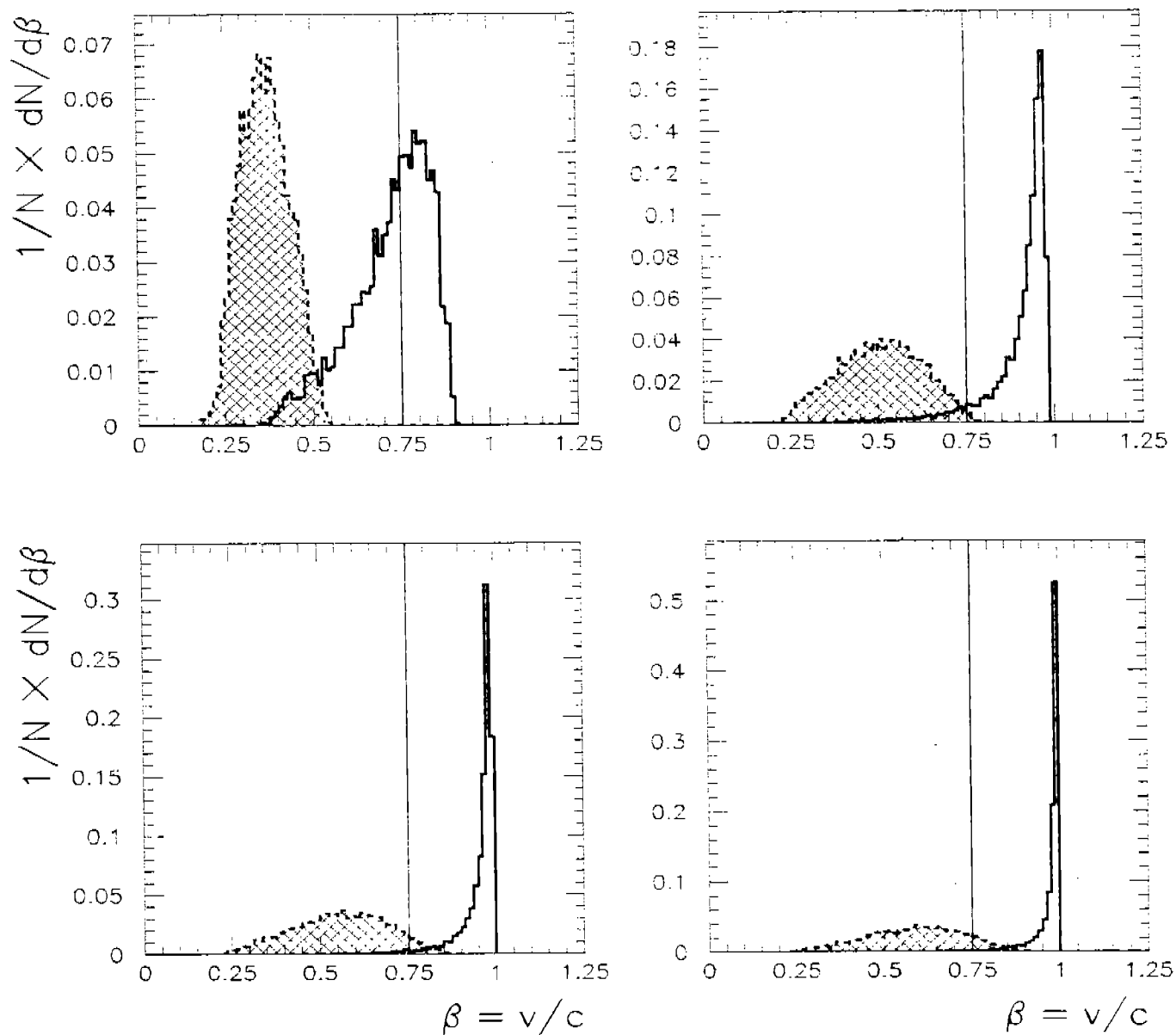## Velocity distributions for pions and protons



Figure 10: Normalized $\beta$ distributions for protons (dashed histogram) and pions (filled-in histogram) for four slices in $E_\gamma$. (upper left) $E_\gamma = 0.5$ GeV. (upper right) $E_\gamma = 1.0$ GeV, (lower left) $E_\gamma = 1.5$ GeV, and (lower right) $E_\gamma = 2.1$ GeV. The vertical line is the $\beta \geq 0.75$ cutoff.
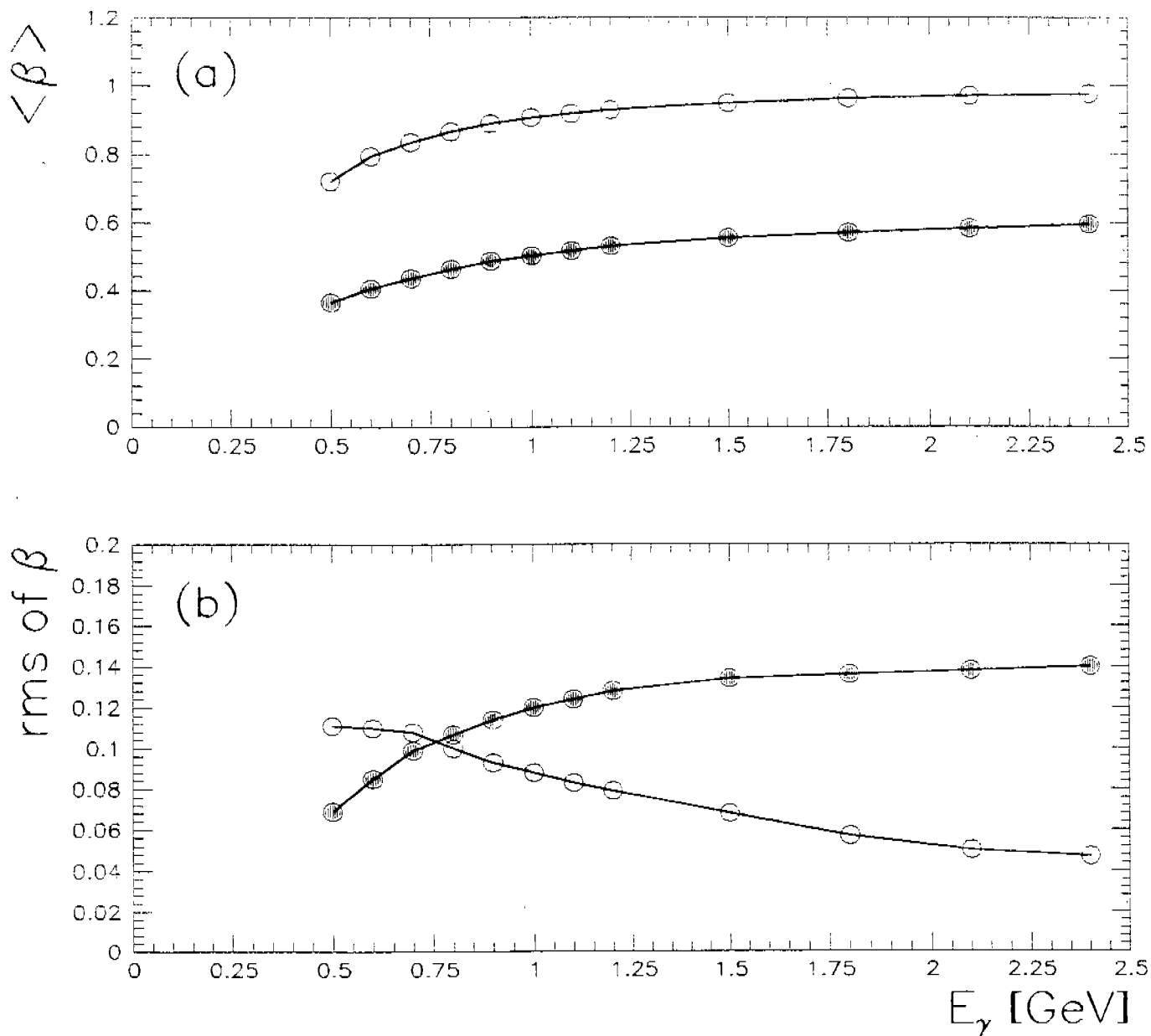
Figure 11: $\beta$ distribution parameters for pions ($\circ$) and protons ($\bullet$) as a function of $E_\gamma$. **(a)** Average $\beta$, and **(b)** rms spread. No velocity cuts have been imposed.

serve to calibrate the TOF system. In Fig. 12a-c, the uncertainty in the timing of the pion for a path length of 400 cm is plotted as a function of $E_\gamma$, and cuts on $|\Delta E|$, and $\beta$.

We take Fig. 12a as our representative plot for $\sigma_{\Delta t}$, where we have fixed the energy balance to be less than or equal to 5 MeV. A fully instrumented tagger will measure the energy of the photon in the range from 0.20 to 0.95 of the electron beam energy $E_o = 2.4$ GeV, which will allow us to measure photons in the energy range of $0.48 \leq E_\gamma \leq 2.28$ GeV. The expected intrinsic resolution of the TOF scintillators is 150 psec. The calibrating pion clearly should not have a timing uncertainty in excess of this value. Referring to Fig. 13 (an expansion of Fig. 12a) we see that $\sigma_{\Delta t} < 100$ psec for $E_\gamma > 1.00$ GeV when the the velocity cut of $\beta_\pi \geq 0.75$ is imposed. We therefore will be able to use tagged photons with energies in the range of 0.42 to 0.95 of the incident electron beam energy for calibrating the TOF system with relativistic pion tracks.

## 3.4 Backgrounds

Because we measure three charged particles in the final state, and do not employ the TOF scintillators to mass identify the final-state particles, we expect the primary contributions to the background to be

$$\gamma + p \rightarrow p + \pi^+ + \pi^- + \pi^\circ$$
$$\text{and}$$
$$\gamma + p \rightarrow n + \pi^+ + \pi^+ + \pi^-.$$
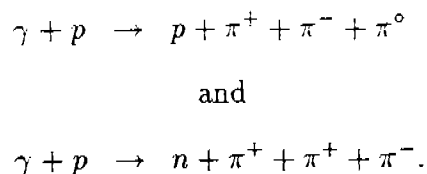
Like the case for our acceptance studies of the signal reaction, our background processes were binned in terms of:

$E_\gamma$:  0.5, 0.6, 0.7, 0.8, 0.9, 1.0, 1.1, 1.2, 1.5, 1.8, 2.1, and 2.4 GeV

$|\Delta E|$:  5, 10, and 20 MeV

$\beta_{cut}$:  0 and 0.75

Again we have $12 \times 3 \times 3 = 72$ bins, in all, and for each bin, we again generated 50 000 events.

We make the same cuts on the background events as for the signal ($\gamma p \rightarrow p\pi^+\pi^-$). That is to say, each track of the three final-state charged particles is measured in all three wire chambers, and $|\Delta E| < E_{min}$. In Figs. 14a–c (Figs. 15a–c) we plot the acceptances for the reaction $\gamma p \rightarrow p\pi^+\pi^-\pi^\circ$ ($\gamma p \rightarrow n\pi^+\pi^+\pi^-$), after all cuts have been applied, as a function of $E_\gamma$, $|\Delta E|$, and $\beta_{cut}$. We first
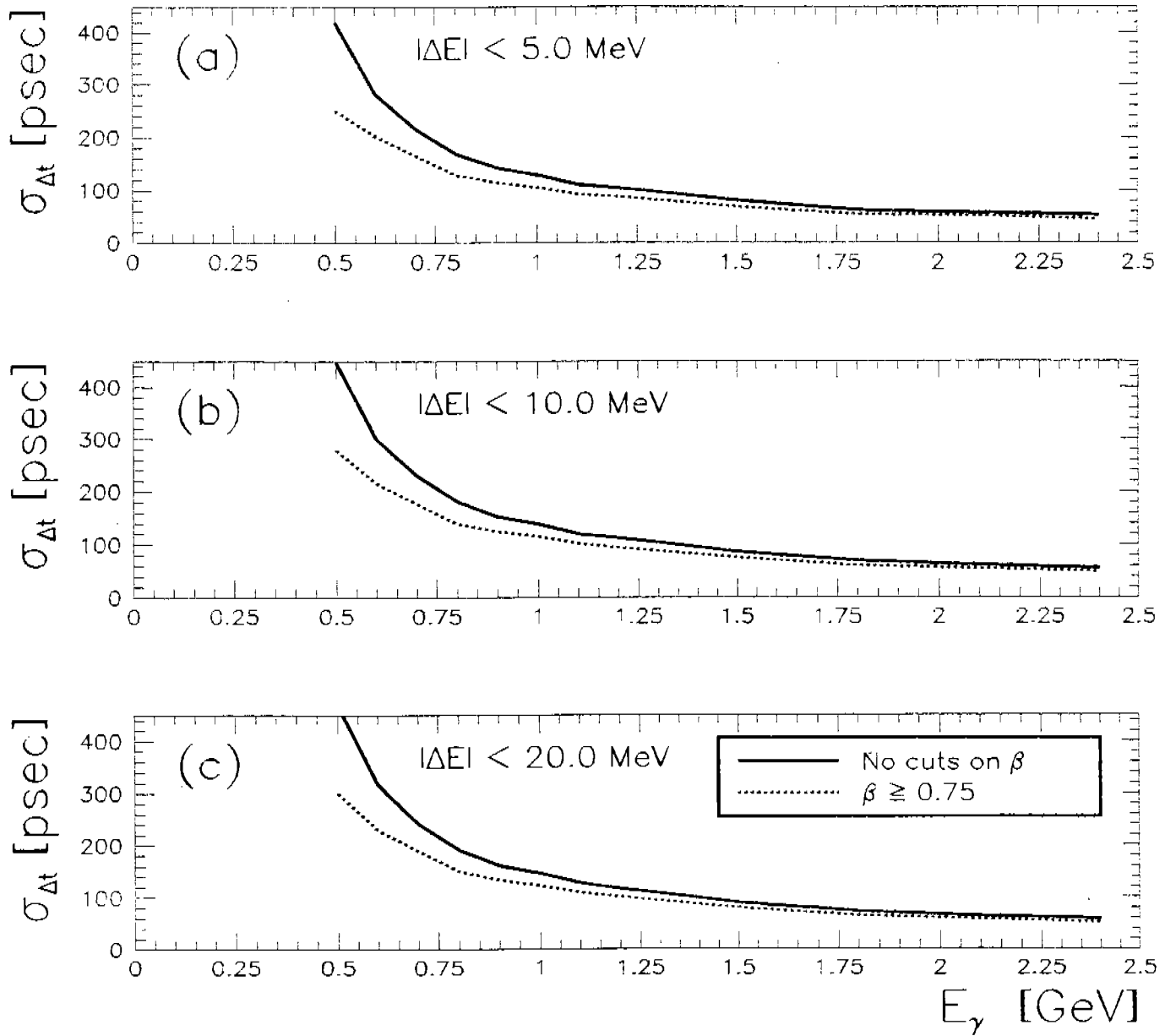
# Timing Uncertainty of π Track



Figure 12: Resolution of the $\pi$ track's timing, $\sigma_{\Delta t}$, for pions arising from $\gamma p \rightarrow p\pi^+\pi^-$ as a function of incident photon energy and for energy balance cuts of (a) $|\Delta E| < 5$ MeV, (b) $|\Delta E| < 10$ MeV, and (c) $|\Delta E| < 20$ MeV. The path length is taken to be 400 cm.
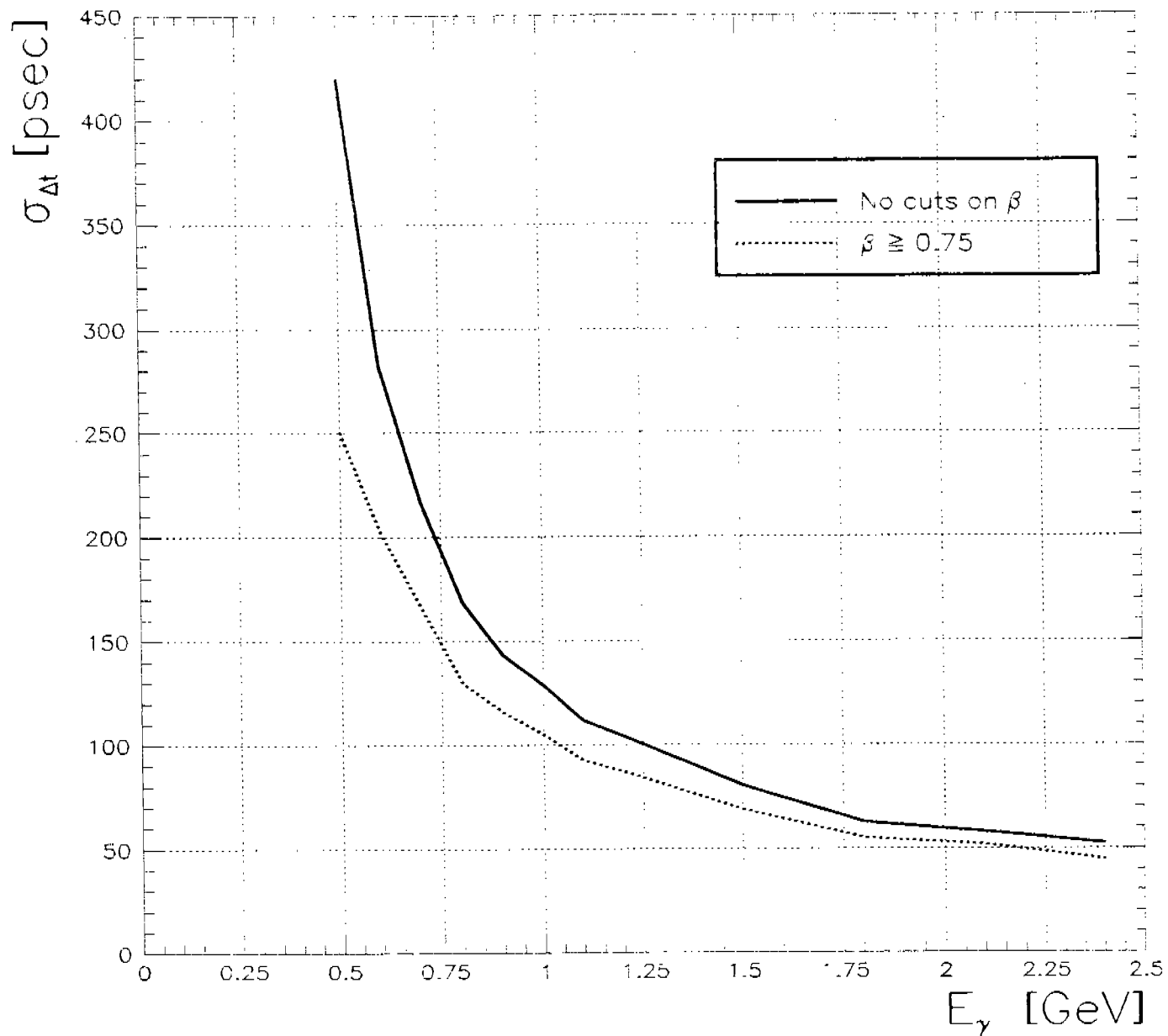
Figure 13: Resolution of the $\pi$ track's timing, $\sigma_{\Delta t}$, for pions arising from $\gamma p \to p\pi^+\pi^-$ as a function of incident photon energy for energy balance of $|\Delta E| < 5$ MeV. This figure is an expansion of Fig. 12a

Figure 14: Acceptance of the signal ($\gamma p \to p\pi^+\pi^-\pi^\circ$) as a function of incident photon energy and tracking angular resolution for (a) $|\Delta E| < 5$ MeV, (b) $|\Delta E| < 10$ MeV, and (c) $|\Delta E| < 20$ MeV.
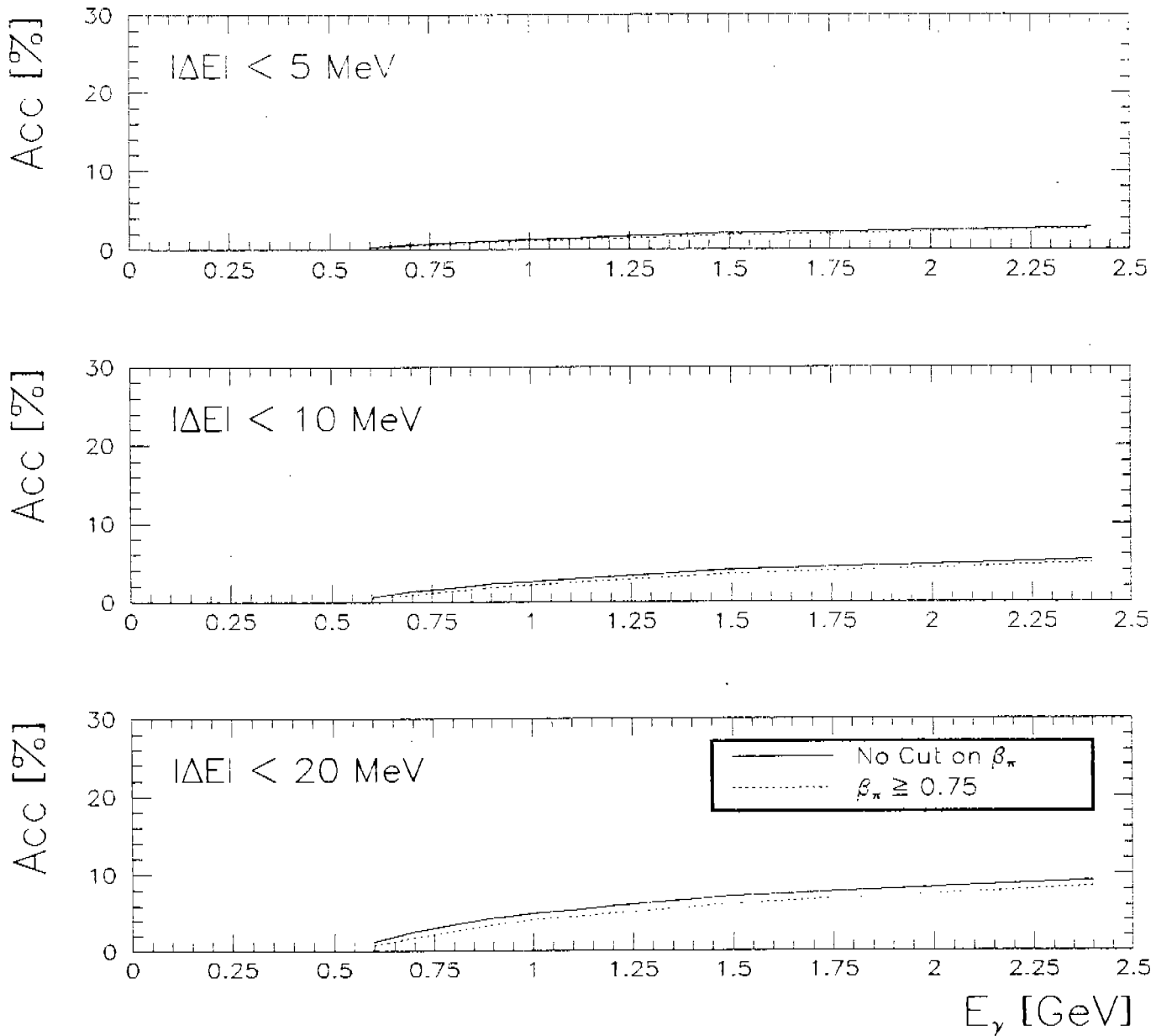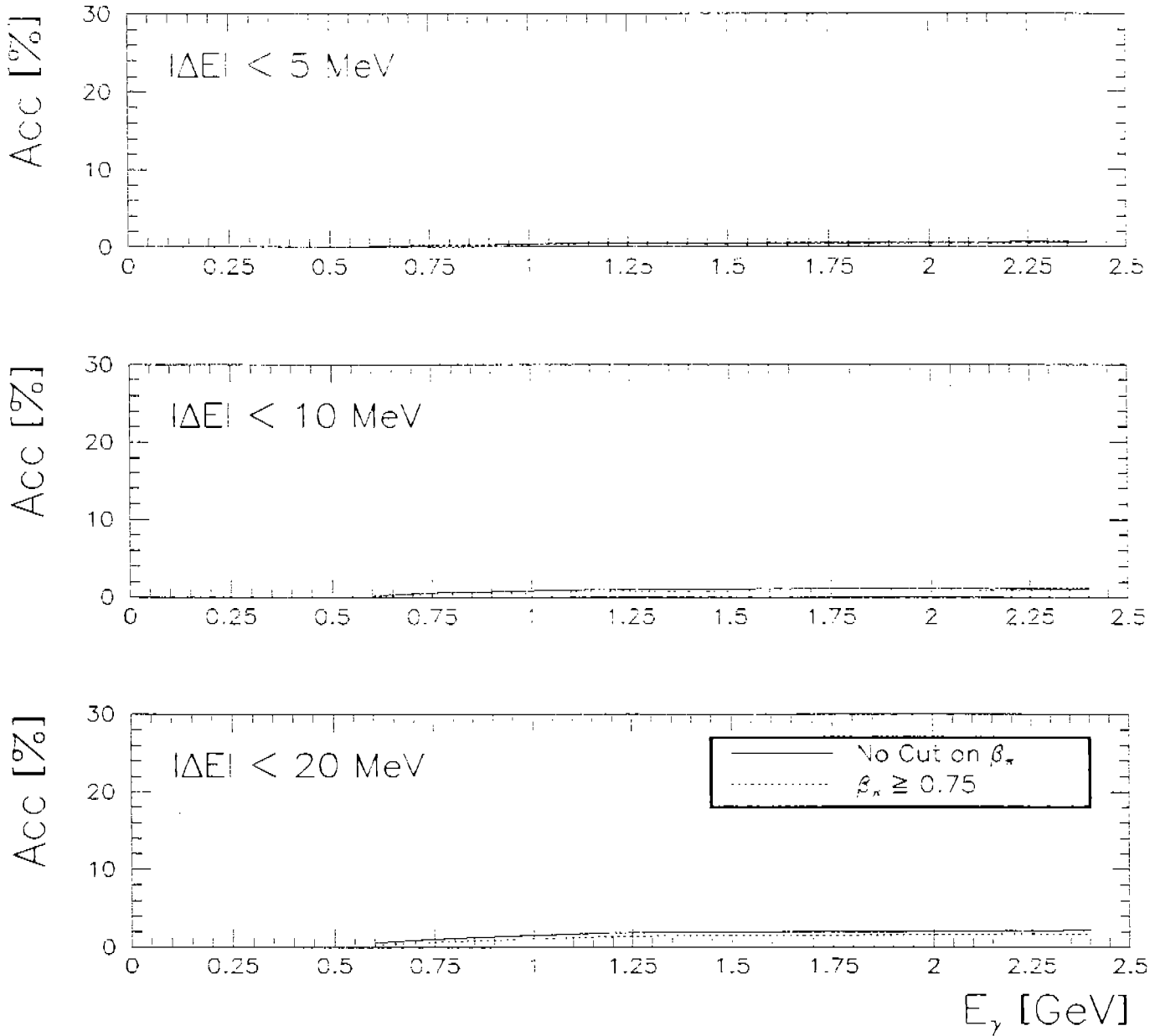
## π Acceptance from p(γ,π⁺π⁺π⁻)n



Figure 15: Acceptance of the signal ($\gamma p \rightarrow n\pi^+\pi^+\pi^-$) as a function of incident photon energy and tracking angular resolution for (a) $|\Delta E| < 5$ MeV, (b) $|\Delta E| < 10$ MeV, and (c) $|\Delta E| < 20$ MeV.

observe that the acceptance of the background is independent of the velocity cut $\beta_\pi$. Secondly, the signal-to-noise ratio is of the order of 10:1 (20:1) for the background process $\gamma p \rightarrow p\pi^+\pi^-\pi^\circ$ ($\gamma p \rightarrow n\pi^+\pi^+\pi^-$) with $|\Delta E| < 5$ MeV over the photon energy range of $1.0 < E_\gamma < 2.25$ GeV. We remark that once we fold in the cross section, the signal-to-noise ratio will be enhanced still further, as is discussed in detail in the next section.

# 4  Counting Rate Estimates

In this section we estimate the counting rates for both the signal reaction ($\gamma p \rightarrow p\pi^+\pi^-$) and the background reactions ($\gamma p \rightarrow p\pi^+\pi^-\pi^\circ$ and $\gamma p \rightarrow n\pi^+\pi^+\pi^-$). From the relationship

$$N_{\text{evts}} = \Phi N_{\text{nucl}}\sigma, \tag{16}$$

where $\Phi$ is the tagged-photon rate and is taken to be $10^7$ Hz,[1] the number of target nuclei per unit area, $N_{\text{nucl}} = N_A \rho \tau$, $\rho\tau$ is equal to $(0.071 \text{ g/cm}^3)(12 \text{ cm})$, and $\sigma$ is the total cross section. In Table 2 we tabulate the total cross sections as a function of incident photon energy for both the signal and background reactions. We obtained the cross sections of multiple pion photoproduction from Fig. 2 of reference [4].

The energy spectrum, $dN/dk$, of the bremsstrahlung photons is nearly proportional to the reciprocal of the photon energy, $k$. We define the normalized fraction of events falling within a certain photon energy bin as

$$f_{\Delta E_\gamma} = \frac{\displaystyle\int_{E_i}^{E_{i+1}} \frac{dk}{k}}{\displaystyle\int_{0.20E_0}^{0.95E_0} \frac{dk}{k}}, \tag{17}$$

where $E_i$ is the photon energy at the $i$th bin, and $E_0$ is the electron beam energy. For our calculations, we have set $E_0 = 2.4$ GeV. In Table 3, we tabulate the number of events produced and accepted per photon energy bin for both the signal ($\gamma p \rightarrow p\pi^+\pi^-$) and the background ($\gamma p \rightarrow p\pi^+\pi^-\pi^\circ$ and $\gamma p \rightarrow n\pi^+\pi^+\pi^-$) reactions. We define the number of events produced per

---

[1] We have not accounted for untagged photons nor for accidental coincidences in this study. The majority of the untagged photons will be low energy. Because our acceptance cuts require that there be a highly relativistic pion in the final state, and that the energy of the incident photon exceed 1 GeV, we doubt untagged photons will plague our overall counting rate of accepted particles.

Table 2: Total cross sections [4] as a function of $E_\gamma$ for the signal and background reactions.

| $E_\gamma$ [GeV] | $\sigma_{\gamma p \to p\pi^+\pi^-}$ [$\mu$b] | $\sigma_{\gamma p \to p\pi^+\pi^-\pi^0}$ [$\mu$b] | $\sigma_{\gamma p \to n\pi^+\pi^+\pi^-}$ [$\mu$b] |
|---|---|---|---|
| 0.5 | 25 | 0 | 0 |
| 0.6 | 60 | 0 | 0 |
| 0.7 | 75 | 3 | 0 |
| 0.8 | 75 | 5 | 3 |
| 0.9 | 80 | 5 | 4 |
| 1.0 | 75 | 8 | 5 |
| 1.1 | 70 | 10 | 6 |
| 1.2 | 60 | 15 | 8 |
| 1.5 | 55 | 25 | 10 |
| 1.8 | 45 | 25 | 10 |
| 2.1 | 40 | 25 | 10 |
| 2.4 | 35 | 25 | 10 |

second per photon energy bin as

$$
\begin{aligned}
N_{\mathrm{prod}} &= f_{\Delta E_\gamma} N_{\mathrm{evts}} \\
&= f_{\Delta E_\gamma} \Phi N_{\mathrm{nucl}} \sigma.
\end{aligned} \tag{18}
$$

Similarly, we define the number of events accepted per second per photon energy bin having at least one highly relativistic pion as

$$
\begin{aligned}
N_{\mathrm{acc}} &= f_{\Delta E_\gamma} N_{\mathrm{meas}} \\
&= f_{\Delta E_\gamma} \varepsilon \Phi N_{\mathrm{nucl}} \sigma.
\end{aligned} \tag{19}
$$

In Fig. 16 we plot $N_{\mathrm{acc}}$ for both signal and background events as a function of $E_\gamma$. We note that there is absolutely no noise for $E_\gamma < 0.65$ GeV. We define the signal-to-noise ratio as

$$
\mathrm{SNR} = \frac{N_{\mathrm{acc}}^{\gamma p \to p\pi^+\pi^-}}{N_{\mathrm{acc}}^{\gamma p \to p\pi^+\pi^-\pi^0} + N_{\mathrm{acc}}^{\gamma p \to n\pi^+\pi^+\pi^-}}. \tag{20}
$$

In Fig. 17 the signal-to-noise ratio as a function of $E_\gamma$ is plotted. For $1.0 < E_\gamma < 2.25$ GeV, the signal-to-noise ratio is greater that 10:1. We observe, furthermore, that 70% of the accepted signal events are within this energy range.

Table 3: Tabulation of the number of events produced ($N_{\mathrm{prod}} = f_{\Delta E_\gamma} \Phi N_{\mathrm{nucl}} \sigma$) and accepted ($N_{\mathrm{acc}} = f_{\Delta E_\gamma} \varepsilon \Phi N_{\mathrm{nucl}} \sigma$) per photon energy bin (bin width $= 100$ MeV) for the signal and the background reactions. SNR is the signal-to-noise ratio and is defined in the text.

| $E_\gamma$ [GeV] | $f_{\Delta E_\gamma}$ | $\gamma p \to p\pi^+\pi^-$ | | $\gamma p \to p\pi^+\pi^-\pi^0$ | | $\gamma p \to n\pi^+\pi^+\pi^-$ | | SNR |
|---|---|---|---|---|---|---|---|---|
| | | $N_{\mathrm{prod}}$ | $N_{\mathrm{acc}}$ | $N_{\mathrm{prod}}$ | $N_{\mathrm{acc}}$ | $N_{\mathrm{prod}}$ | $N_{\mathrm{acc}}$ | |
| $0.55 \le E_\gamma < 0.65$ | .1072 | 33.0 | 2.6 | — | — | — | — | — |
| $0.65 \le E_\gamma < 0.75$ | .0918 | 35.3 | 3.9 | 1.5 | .008 | — | — | 490 |
| $0.75 \le E_\gamma < 0.85$ | .0830 | 32.0 | 4.3 | 2.4 | .016 | 1.3 | .003 | 226 |
| $0.85 \le E_\gamma < 0.95$ | .0714 | 29.3 | 4.5 | 2.7 | .017 | 1.5 | .003 | 225 |
| $0.95 \le E_\gamma < 1.05$ | .0642 | 24.7 | 4.2 | 3.2 | .030 | 1.6 | .005 | 120 |
| $1.05 \le E_\gamma < 1.15$ | .0584 | 21.0 | 3.6 | 3.0 | .038 | 1.8 | .007 | 80 |
| $1.15 \le E_\gamma < 1.25$ | .0535 | 16.5 | 3.2 | 4.1 | .058 | 2.1 | .009 | 48 |
| $1.25 \le E_\gamma < 1.35$ | .0494 | 14.7 | 2.9 | 4.5 | .072 | 2.6 | .010 | 35 |
| $1.35 \le E_\gamma < 1.45$ | .0459 | 13.3 | 2.6 | 5.0 | .085 | 2.4 | .009 | 28 |
| $1.45 \le E_\gamma < 1.55$ | .0428 | 12.1 | 2.5 | 5.5 | .102 | 2.2 | .009 | 22 |
| $1.55 \le E_\gamma < 1.65$ | .0401 | 10.7 | 2.2 | 5.1 | .099 | 2.1 | .009 | 22 |
| $1.65 \le E_\gamma < 1.75$ | .0378 | 9.5 | 2.0 | 4.9 | .098 | 2.0 | .009 | 20 |
| $1.75 \le E_\gamma < 1.85$ | .0357 | 8.2 | 1.7 | 5.3 | .096 | 1.8 | .009 | 16 |
| $1.85 \le E_\gamma < 1.95$ | .0338 | 7.5 | 1.5 | 4.5 | .094 | 1.7 | .008 | 15 |
| $1.95 \le E_\gamma < 2.05$ | .0321 | 6.9 | 1.4 | 4.1 | .093 | 1.6 | .008 | 14 |
| $2.05 \le E_\gamma < 2.15$ | .0306 | 6.3 | 1.3 | 3.9 | .092 | 1.5 | .007 | 13 |
| $2.15 \le E_\gamma < 2.25$ | .0292 | 5.7 | 1.1 | 3.8 | .092 | 1.5 | .007 | 11 |
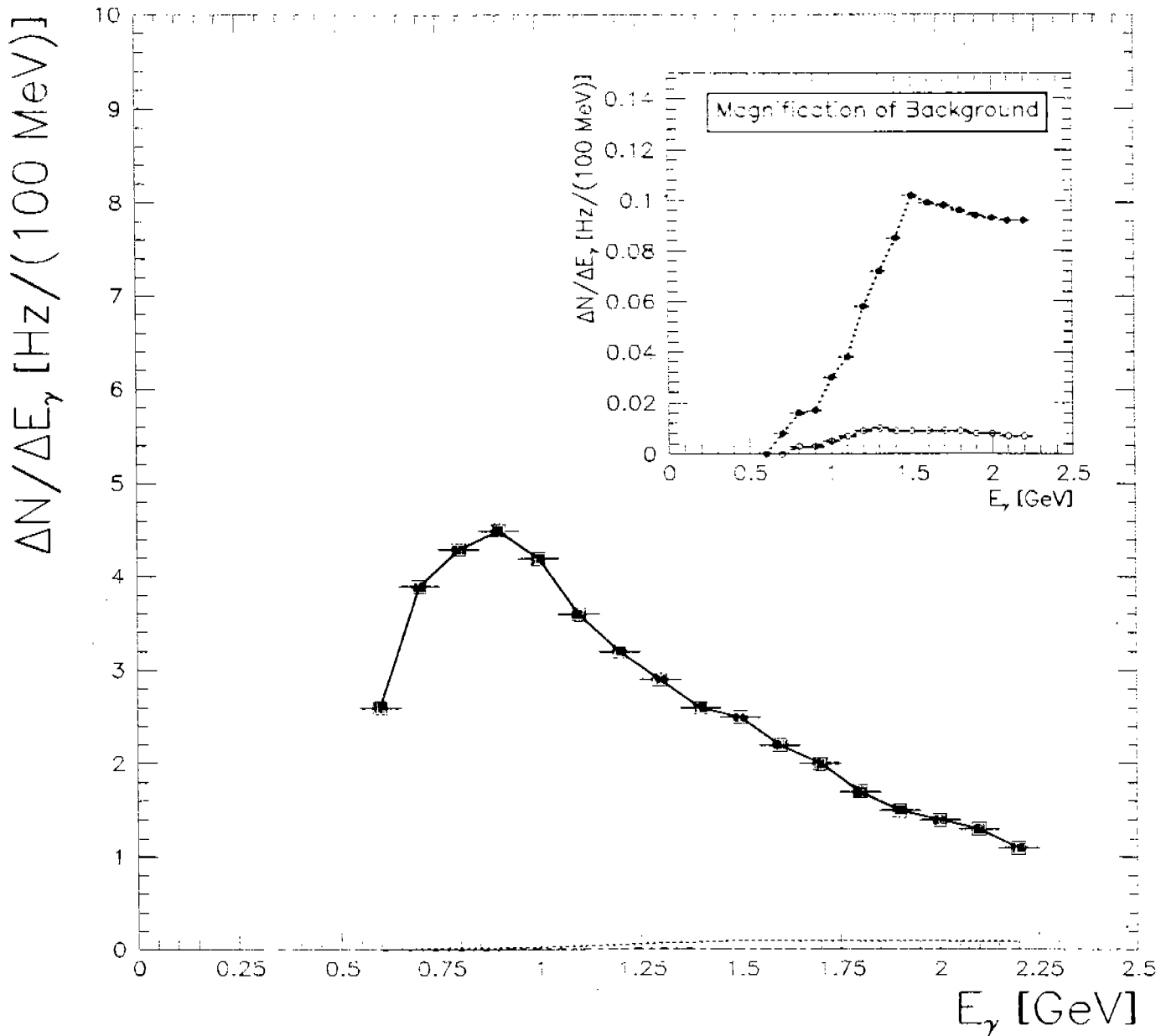
Figure 16: Number of events accepted per second in each 100 MeV energy bin as a function of $E_\gamma$ for both signal and background processes. The inset is a magnification of the background processes. The **solid line** is for the signal ($\gamma p \to p\pi^+\pi^-$), and the background reactions are represented by the **dotted line** for $\gamma p \to p\pi^+\pi^-\pi^\circ$, and by the **dash-dotted line** for $\gamma p \to n\pi^+\pi^+\pi^-$.
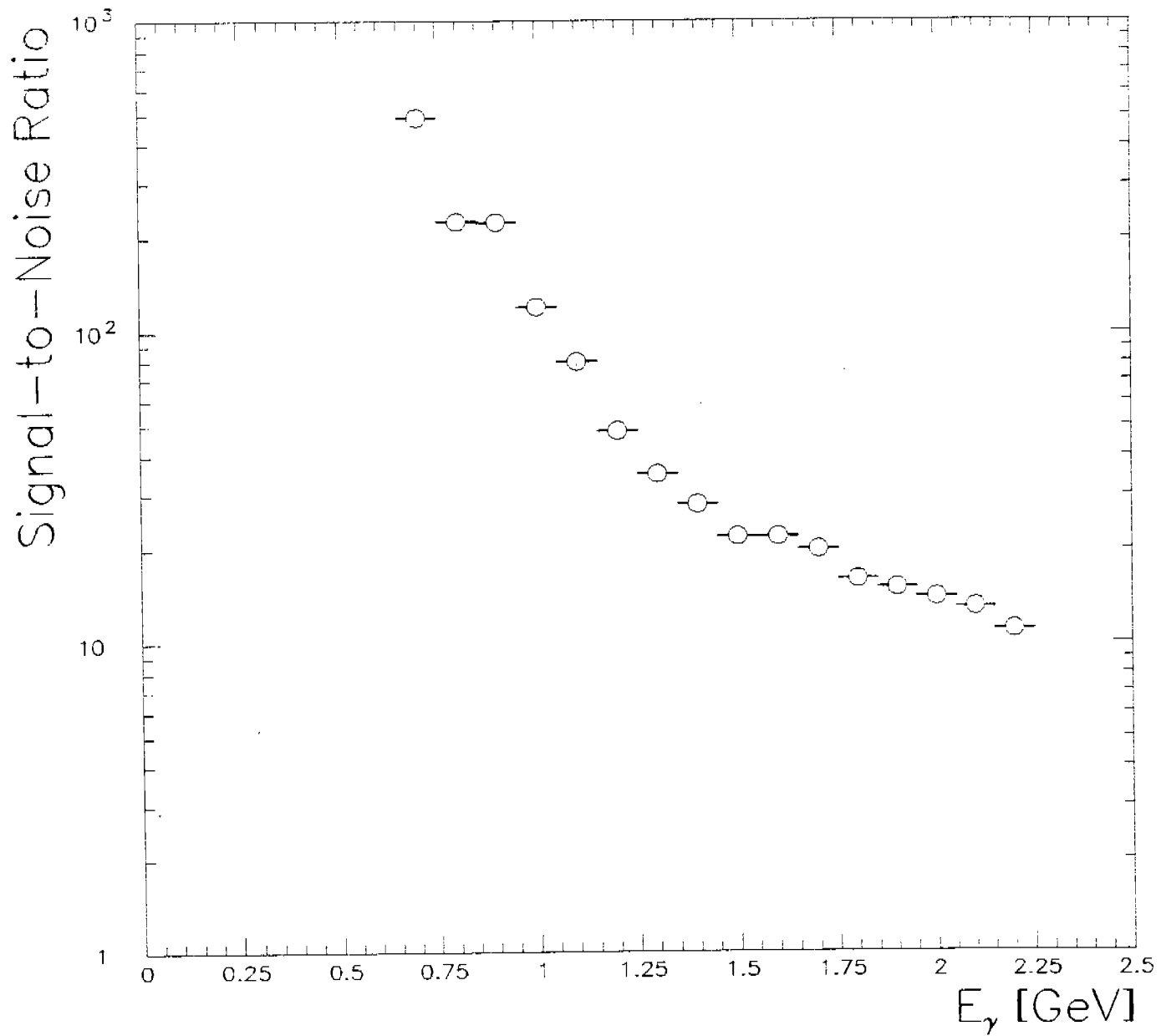
Figure 17: Signal-to-noise ratio as a function of incident photon energy, $E_\gamma$. The noise is the sum of the background events ($\gamma p \to p\pi^+\pi^-\pi^\circ$ and $\gamma p \to n\pi^+\pi^+\pi^-$) accepted per second in bin widths of 100 MeV, and similarly for the signal ($\gamma p \to p\pi^+\pi^-$).

Table 4: Tabulation of the counting rate in the backward region of the TOF system binned in terms of the incident photon energy, $E_\gamma$, and polar angle, $\theta$.

| $E_\gamma$ [GeV] | $90° < \theta \leq 100°$ [Hz] | $100° < \theta \leq 110°$ [Hz] | $110° < \theta \leq 120°$ [Hz] | $120° < \theta \leq 130°$ [Hz] | $130° < \theta \leq 140°$ [Hz] |
|---|---|---|---|---|---|
| $0.55 \leq E_\gamma < 0.65$ | $1.65 \times 10^{-2}$ | $9.69 \times 10^{-3}$ | $6.09 \times 10^{-3}$ | $4.05 \times 10^{-3}$ | $1.44 \times 10^{-3}$ |
| $0.75 \leq E_\gamma < 0.85$ | $1.53 \times 10^{-2}$ | $1.06 \times 10^{-2}$ | $6.00 \times 10^{-3}$ | $4.59 \times 10^{-3}$ | $1.61 \times 10^{-3}$ |
| $0.85 \leq E_\gamma < 0.95$ | $1.23 \times 10^{-2}$ | $9.00 \times 10^{-3}$ | $4.40 \times 10^{-3}$ | $4.44 \times 10^{-3}$ | $7.29 \times 10^{-4}$ |
| $0.95 \leq E_\gamma < 1.05$ | $1.00 \times 10^{-2}$ | $6.17 \times 10^{-3}$ | $4.24 \times 10^{-3}$ | $3.53 \times 10^{-3}$ | $8.01 \times 10^{-4}$ |
| $1.05 \leq E_\gamma < 1.15$ | $8.28 \times 10^{-3}$ | $4.61 \times 10^{-3}$ | $3.00 \times 10^{-3}$ | $1.91 \times 10^{-3}$ | $6.37 \times 10^{-4}$ |
| $1.15 \leq E_\gamma < 1.25$ | $6.66 \times 10^{-3}$ | $3.78 \times 10^{-3}$ | $1.86 \times 10^{-3}$ | $1.83 \times 10^{-3}$ | $3.78 \times 10^{-4}$ |
| $1.25 \leq E_\gamma < 1.35$ | $4.93 \times 10^{-3}$ | $3.01 \times 10^{-3}$ | $1.52 \times 10^{-3}$ | $1.35 \times 10^{-3}$ | $3.12 \times 10^{-4}$ |
| $1.35 \leq E_\gamma < 1.45$ | $3.20 \times 10^{-3}$ | $2.41 \times 10^{-3}$ | $1.18 \times 10^{-3}$ | $8.68 \times 10^{-4}$ | $2.45 \times 10^{-4}$ |
| $1.45 \leq E_\gamma < 1.55$ | $3.08 \times 10^{-3}$ | $2.32 \times 10^{-3}$ | $1.14 \times 10^{-3}$ | $8.35 \times 10^{-4}$ | $2.36 \times 10^{-4}$ |
| $1.55 \leq E_\gamma < 1.65$ | $2.71 \times 10^{-3}$ | $2.04 \times 10^{-3}$ | $1.00 \times 10^{-3}$ | $7.35 \times 10^{-4}$ | $2.07 \times 10^{-4}$ |
| $1.65 \leq E_\gamma < 1.75$ | $1.81 \times 10^{-3}$ | $1.00 \times 10^{-3}$ | $7.58 \times 10^{-4}$ | $5.00 \times 10^{-4}$ | $1.38 \times 10^{-4}$ |
| $1.75 \leq E_\gamma < 1.85$ | $1.54 \times 10^{-3}$ | $8.50 \times 10^{-4}$ | $6.44 \times 10^{-4}$ | $4.25 \times 10^{-4}$ | $1.17 \times 10^{-4}$ |
| $1.85 \leq E_\gamma < 1.95$ | $1.36 \times 10^{-3}$ | $7.50 \times 10^{-4}$ | $5.69 \times 10^{-4}$ | $3.75 \times 10^{-4}$ | $1.04 \times 10^{-4}$ |
| $1.95 \leq E_\gamma < 2.05$ | $7.56 \times 10^{-4}$ | $6.17 \times 10^{-4}$ | $4.24 \times 10^{-4}$ | $3.53 \times 10^{-4}$ | $1.21 \times 10^{-4}$ |
| $2.05 \leq E_\gamma < 2.15$ | $7.02 \times 10^{-4}$ | $5.32 \times 10^{-4}$ | $3.80 \times 10^{-4}$ | $3.34 \times 10^{-4}$ | $1.12 \times 10^{-4}$ |
| $2.15 \leq E_\gamma < 2.25$ | $5.94 \times 10^{-4}$ | $4.25 \times 10^{-4}$ | $3.21 \times 10^{-4}$ | $3.00 \times 10^{-4}$ | $1.00 \times 10^{-4}$ |
| $0.95 \leq E_\gamma < 2.25$ | $4.56 \times 10^{-2}$ | $2.85 \times 10^{-2}$ | $1.70 \times 10^{-2}$ | $1.33 \times 10^{-2}$ | $3.51 \times 10^{-3}$ |

## 5 Polar Angle Distributions

The polar angle, $\theta$, distribution of the pions is forwardly peaked in the laboratory frame. In Fig. 18, we plot the polar angle distributions normalized by area of the pion for several slices of $E_\gamma$. As $E_\gamma$ increases, the pion track becomes more forwardly peaked. In section 3.3, we found that the incident photon energy must exceed 1 GeV for the timing resolution of the calibrating pion track to be less than 100 psec (cf. Fig. 12). The TOF counters extend from 7° to 140° in polar angle. Because the $\theta$ distribution of the pions is so forwardly peaked, significantly fewer pion tracks will be directed towards the backward regions of the TOF system. In Table 4, we tabulate the counting rate in the backward region of the TOF system as a function of incident photon energy and $\theta$ bin.

## 6 Conclusion

In this **CLAS-NOTE**, we have shown that we can use the fast-moving pions resulting from the reaction $\gamma p \rightarrow p\pi^+\pi^-$ to calibrate the TOF counters. To keep the signal-to-noise ratio greater
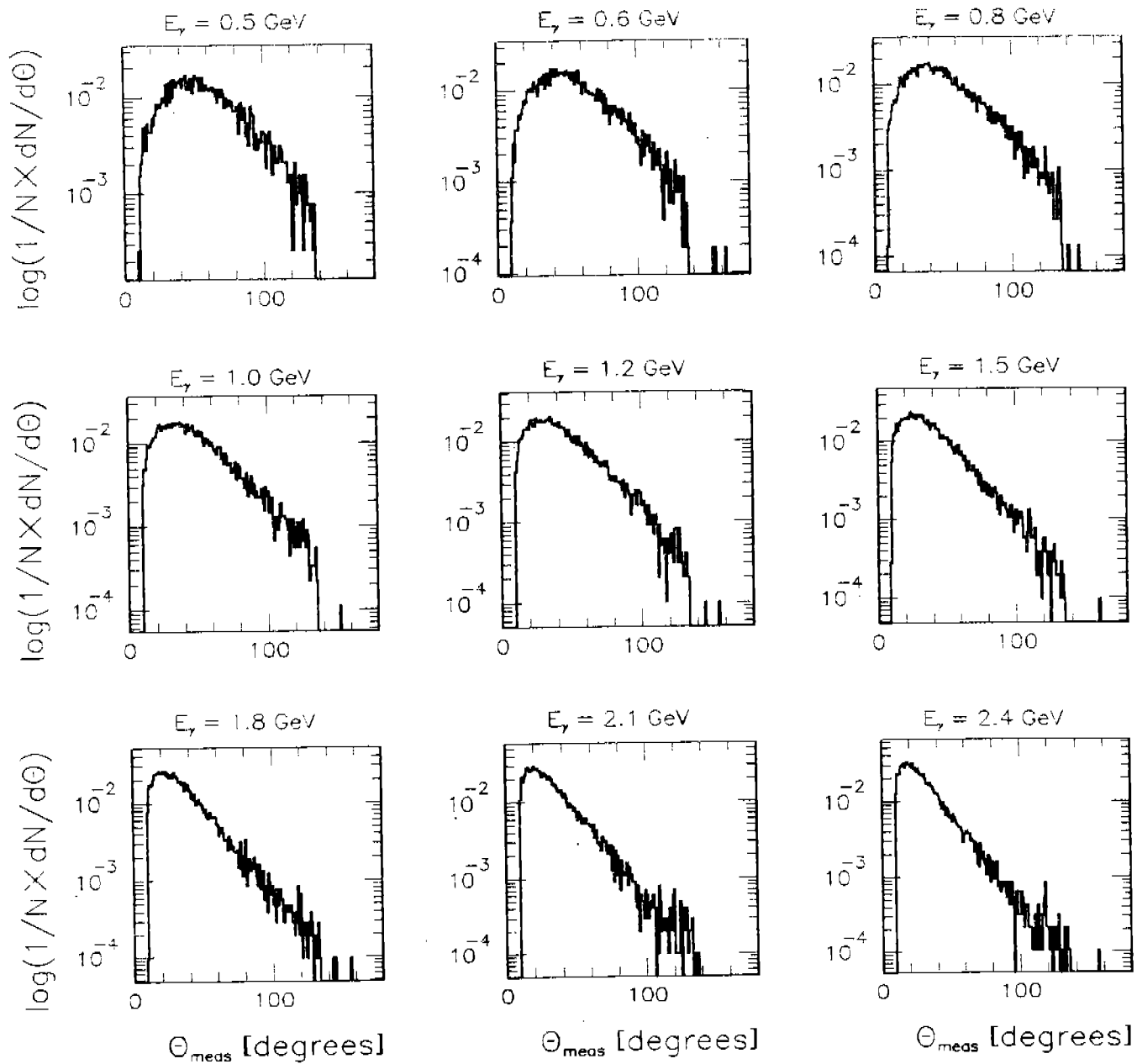
Figure 18: Polar angle distributions of the pion for several slices in $E_\gamma$. The distributions are normalized by area.

than 10:1 and the timing uncertainty of the pion to less than 100 psec, one should use only tagged photons in the energy range of $1.0 < E_\gamma < 2.25$ GeV. Under these conditions we expect a counting rate of approximately 30 accepted events per second. Because of this high counting rate, we will trigger on events that have identically three charged particles in the final state, and have at least one hit in the TOF system. The total beamtime required to calibrate the TOF system is set by the counting rate in the most backward region of the counters. We require 7 **days** to accrue 2000 $\gamma p \to p\pi^+\pi^-$ events, each of which will have one highly relativisitic pion directed in the polar-angle range of $130° < \theta \leq 140°$.

# 7 Acknowledgments

# References

[1] P.L. Cole, "A Generalized **FastMC** for the CLAS," **CLAS-Note** 93-006.

[2] E.S. Smith, "FAST Monte Carlo for the CLAS Detector," **CLAS-Note** 90-003.

[3] E. Anciant, *private communication.*

[4] D. Lūke and P. Sōding, "Multiple Pion Photoproduction in the *s* Channel Resonance Region," *Springer Tracts in Modern Physics,* 59, 39 (1971).